PHYSICAL REVIEW C **95**, 035209 (2017)

First measurement of unpolarized semi-inclusive deep-inelastic scattering cross sections from a ^{3}He target

X. Yan,[1,*] K. Allada,[2,3] K. Aniol,[4] J. R. M. Annand,[5] T. Averett,[6] F. Benmokhtar,[7] W. Bertozzi,[2] P. C. Bradshaw,[6] P. Bosted,[3] A. Camsonne,[3] M. Canan,[8] G. D. Cates,[9] C. Chen,[10] J.-P. Chen,[3] W. Chen,[1] K. Chirapatpimol,[9] E. Chudakov,[3] E. Cisbani,[11,12] J. C. Cornejo,[4] F. Cusanno,[13,†] M. M. Dalton,[9,3] W. Deconinck,[2] C. W. de Jager,[3,9] R. De Leo,[14] X. Deng,[9] A. Deur,[3] H. Ding,[9] P. A. M. Dolph,[9] C. Dutta,[15] D. Dutta,[16] L. El Fassi,[16] S. Frullani,[13,12] H. Gao,[1] F. Garibaldi,[13,12] D. Gaskell,[3] S. Gilad,[2] R. Gilman,[3,17] O. Glamazdin,[18] S. Golge,[8] L. Guo,[19,20] D. Hamilton,[5] O. Hansen,[3] D. W. Higinbotham,[3] T. Holmstrom,[21] J. Huang,[2,19] M. Huang,[1] H. F. Ibrahim,[22] M. Iodice,[23] X. Jiang,[17,19] G. Jin,[9] M. K. Jones,[3] J. Katich,[6] A. Kelleher,[6] W. Kim,[24] A. Kolarkar,[15] W. Korsch,[15] J. J. LeRose,[3] X. Li,[25] Y. Li,[25] R. Lindgren,[9] T. Liu,[1] N. Liyanage,[9] E. Long,[26] H.-J. Lu,[27] D. J. Margaziotis,[4] P. Markowitz,[20] S. Marrone,[14] D. McNulty,[28] Z.-E. Meziani,[29] R. Michaels,[3] B. Moffit,[2,3] C. Muñoz Camacho,[30] S. Nanda,[3] A. Narayan,[16] V. Nelyubin,[9] B. Norum,[9] Y. Oh,[31] M. Osipenko,[32] D. Parno,[33] J.-C. Peng,[34] S. K. Phillips,[35] M. Posik,[29] A. J. R. Puckett,[2,19] X. Qian,[36] Y. Qiang,[1,3] A. Rakhman,[37] R. Ransome,[17] S. Riordan,[9] A. Saha,[3,†] B. Sawatzky,[29,3] E. Schulte,[17] A. Shahinyan,[38] M. H. Shabestari,[9] S. Širca,[39] S. Stepanyan,[3] R. Subedi,[9] V. Sulkosky,[2,3] L.-G. Tang,[10] W. A. Tobias,[9] G. M. Urciuoli,[13] I. Vilardi,[14] K. Wang,[9] B. Wojtsekhowski,[3] Y. Wang,[34] X. Yan,[27] H. Yao,[29] Y. Ye,[27] Z. Ye,[10] L. Yuan,[10] X. Zhan,[2] Y. Zhang,[40] Y.-W. Zhang,[40] B. Zhao,[6] Y. X. Zhao,[27] X. Zheng,[9] L. Zhu,[34,10] X. Zhu,[1] and X. Zong[1]
(Jefferson Lab Hall A Collaboration)

[1]*Duke University, Durham, North Carolina 27708, USA*
[2]*Massachusetts Institute of Technology, Cambridge, Massachusetts 02139, USA*
[3]*Thomas Jefferson National Accelerator Facility, Newport News, Virginia 23606, USA*
[4]*California State University, Los Angeles, Los Angeles, California 90032, USA*
[5]*University of Glasgow, Glasgow G12 8QQ, Scotland, United Kingdom*
[6]*College of William and Mary, Williamsburg, Virginia 23187, USA*
[7]*Duquesne University, Pittsburgh, Pennsylvania 15282, USA*
[8]*Old Dominion University, Norfolk, Virginia 23529, USA*
[9]*University of Virginia, Charlottesville, Virginia 22904, USA*
[10]*Hampton University, Hampton, Virginia 23187, USA*
[11]*INFN, Sezione di Roma, I-00185 Rome, Italy*
[12]*Istituto Superiore di Sanità, I-00161 Rome, Italy*
[13]*INFN, Sezione di Roma, I-00161 Rome, Italy*
[14]*INFN, Sezione di Bari and University of Bari, I-70126 Bari, Italy*
[15]*University of Kentucky, Lexington, Kentucky 40506, USA*
[16]*Mississippi State University, Mississippi 39762, USA*
[17]*Rutgers, The State University of New Jersey, Piscataway, New Jersey 08855, USA*
[18]*Kharkov Institute of Physics and Technology, Kharkov 61108, Ukraine*
[19]*Los Alamos National Laboratory, Los Alamos, New Mexico 87545, USA*
[20]*Florida International University, Miami, Florida 33199, USA*
[21]*Longwood University, Farmville, Virginia 23909, USA*
[22]*Cairo University, Giza 12613, Egypt*
[23]*INFN, Sezione di Roma Tre, I-00146 Rome, Italy*
[24]*Kyungpook National University, Taegu 702-701, Republic of Korea*
[25]*China Institute of Atomic Energy, Beijing, People's Republic of China*
[26]*Kent State University, Kent, Ohio 44242, USA*
[27]*University of Science and Technology of China, Hefei 230026, People's Republic of China*
[28]*University of Massachusetts, Amherst, Massachusetts 01003, USA*
[29]*Temple University, Philadelphia, Pennsylvania 19122, USA*
[30]*Université Blaise Pascal/IN2P3, F-63177 Aubière, France*
[31]*Seoul National University, Seoul, South Korea*
[32]*INFN, Sezione di Genova, I-16146 Genova, Italy*
[33]*Carnegie Mellon University, Pittsburgh, Pennsylvania 15213, USA*
[34]*University of Illinois, Urbana-Champaign, Illinois 61801, USA*
[35]*University of New Hampshire, Durham, New Hampshire 03824, USA*
[36]*Physics Department, Brookhaven National Laboratory, Upton, New York, USA*
[37]*Syracuse University, Syracuse, New York 13244, USA*
[38]*Yerevan Physics Institute, Yerevan 375036, Armenia*

2469-9985/2017/95(3)/035209(27)

[39] *University of Ljubljana, SI-1000 Ljubljana, Slovenia*
[40] *Lanzhou University, Lanzhou 730000, Gansu, People's Republic of China*

(Received 7 October 2016; revised manuscript received 8 January 2017; published 24 March 2017)

The unpolarized semi-inclusive deep-inelastic scattering (SIDIS) differential cross sections in $^3\mathrm{He}(e,e'\pi^{\pm})X$ have been measured for the first time in Jefferson Lab experiment E06-010 with a 5.9 GeV e^- beam on a ^{3}He gas target. The experiment focuses on the valence quark region, covering a kinematic range $0.12 < x_{bj} < 0.45$, $1 < Q^2 < 4$ (GeV/c)^2, $0.45 < z_h < 0.65$, and $0.05 < P_t < 0.55$ GeV/c. The extracted SIDIS differential cross sections of $\pi^{\pm}$ production are compared with existing phenomenological models while the ^{3}He nucleus approximated as two protons and one neutron in a plane-wave picture, in multidimensional bins. Within the experimental uncertainties, the azimuthal modulations of the cross sections are found to be consistent with zero.

DOI: 10.1103/PhysRevC.95.035209

I. INTRODUCTION

One of the main goals in nuclear and particle physics is to unravel ultimately the nucleon structure in terms of quarks and gluons, the fundamental degrees of freedom of quantum chromodynamics (QCD). Due to the nonperturbative nature of QCD at hadronic scales, it is not possible yet to calculate the structures of hadrons directly from first principles of QCD. The lepton-nucleon and lepton-nucleus deep inelastic scattering is an important experimental approach and has been widely employed for more than 40 years. During the last decade or so, both experimental and theoretical studies have revealed the nontrivial effects of quark intrinsic transverse momentum, especially spin-related, probed by the semi-inclusive deep-inelastic scattering (SIDIS) processes.

In polarized and unpolarized SIDIS processes, azimuthal modulations of cross sections were found to be sizable [1–4]. The intrinsic transverse momenta of the quarks are expected to play an important role in the observed modulations [5,6]. To incorporate the intrinsic transverse momentum carried by the partons in the description of the SIDIS processes, transverse momentum dependent (TMD) parton distribution functions (PDFs) and fragmentation functions (FFs) were proposed [7,8]. TMD PDFs and FFs include dependence on the transverse momentum of the partons in addition to the longitudinal momentum used in the traditional one-dimensional PDFs and FFs and can provide a more complete understanding of the nucleon structure. A TMD factorization formalism was developed, incorporating the TMD PDFs and FFs [9–12]. Within the TMD factorization framework, plus additional simplifications and assumptions, the 18 structure functions comprising the SIDIS differential cross section are expressed as the convolutions of TMD PDFs and FFs [13] (naive x-z factorization). TMD PDFs and FFs have been parametrized and utilized in the phenomenological studies of the world data of SIDIS and e^+e^- annihilation [14–17]. An example showing the power of this factorization scheme is the agreement between the model description and the experiment for the Sivers and Collins effects [14]. The Sivers effect emerges from the convolution of the Sivers TMD PDF and the unpolarized TMD FF. The Collins effect is from the convolution of the transversity TMD PDF and the Collins TMD FF. Sivers and Collins effects are related to different azimuthal modulations in SIDIS differential cross sections with transversely polarized nucleons [13,14]. Nontrivial azimuthal modulations in unpolarized SIDIS processes arise from the convolution of unpolarized TMD PDF and FF with factors involving the quark intrinsic transverse momentum, known as the Cahn effect [18], and the convolution of the Boer–Mulders function and the Collins function, known as the Boer–Mulders effect [8]. Various TMD PDFs provide valuable anatomy of the nucleon structure. For instance, the Boer–Mulders TMD PDF describes the distribution of transversely polarized quarks inside an unpolarized nucleon [14].

While factorization originates in the high-energy limit ($Q \gg \Lambda_{\mathrm{QCD}}$ or $Q \gg M_{\mathrm{nucleon}}$) [19,20], and at low Q^2 the description using hadronic degrees of freedom is more widely used [21], the applicability of the quark-parton model with factorization in modest Q^2 ranges has been observed in quark-hadron duality [22,23]. One needs to note that, at modest Q^2 ranges, higher-twist terms suppressed by powers of $(1/Q)$ would be larger than those in the range of large Q^2 and could bring non-negligible effects [15].

While SIDIS measurements on the proton have been carried out by a number of experiments [14–17,22–27] and more data will be available, SIDIS data on the neutron are rather limited. Since there is no stable neutron target, using a polarized ^{3}He target as an effective polarized neutron target for experimental studies related to the spin structure of the neutron is uniquely advantageous, due to the dominant neutron spin contribution to the ^{3}He spin [28]. The SIDIS experiment E06-010 in Hall A of Jefferson Lab (JLab) was carried out with a 5.9 GeV polarized electron beam and a transversely polarized ^{3}He target between October 2008 and February 2009. The experiment covered a kinematic range $0.12 < x_{bj} < 0.45$, $1 < Q^2 < 4$ (GeV/c)^2, $0.45 < z_h < 0.65$, and $0.05 < P_t < 0.55$ GeV/c. Studies on the data of E06-010 for single-spin asymmetries (SSAs) and double-spin asymmetries (DSAs) have been carried out [29–32]. These first SIDIS asymmetry results from ^{3}He as an effective neutron target were related to TMD PDFs such as transversity, Sivers, pretzelosity, trans-helicity (g_{1T}^q), and TMD FFs such as Collins.

The unpolarized SIDIS differential cross section, while the spin-dependent azimuthal modulations are canceled,

---

[*] xy33@phy.duke.edu

[†] Deceased.

still involves nontrivial modulations from the Cahn and Boer–Mulders effects. The unpolarized SIDIS differential cross section in the quark-parton model as well as the parametrization of the related TMD PDFs and FFs are presented in Sec. II. As in the studies of the world data [5,15–17], the SIDIS cross section is expressed in the functional form based on the quark-parton model with naive x-z factorization, and the transverse momentum dependence is described as a Gaussian distribution. In global analyses fitting different types of data (multiplicities and/or asymmetries) in different kinematic ranges, very different values were extracted for the width of the quark intrinsic transverse momentum $\langle k_\perp^2\rangle$. Namely, $\langle k_\perp^2\rangle$ is at the level of 0.2 GeV^2 in Refs. [5,17], at the level of 0.5 GeV^2 in Ref. [16], and less than 0.05 GeV^2 in Ref. [15]. While the multiplicities and asymmetries from experiments have been fit with ratios of combinations of the theoretical cross sections, as in the studies of the world data [5,15–17], the corresponding study for the absolute cross sections is rather limited.

In addition to the fact that the absolute cross sections provide more complete information than multiplicities and asymmetries (ratios of combinations of the polarized and unpolarized cross sections), TMD evolution also has a much stronger effect on the absolute cross sections [33]. In recent years, the unpolarized SIDIS processes have attracted considerable interest due to providing special insights into the TMD evolution effect [34].

In this paper, using the E06-010 experimental data, we present the first extraction of the unpolarized SIDIS differential cross sections from a ^{3}He target, comparisons with different models, the study of azimuthal modulations in the extracted cross sections, and the constraints on the phenomenological parameters from the data in this study. In this paper, the units GeV$/c$ and GeV are not discriminated for conciseness of expressions.

II. QUARK-PARTON MODEL AND SEMI-INCLUSIVE DEEP-INELASTIC SCATTERING PARAMETRIZATION

The processes of interest are the unpolarized SIDIS $e(l) + N(P) \rightarrow e'(l') + \pi^{\pm}(P_h) + X(P_X)$, where the variables in the parentheses are the four-vector momenta, e is the beam electron, N is the target nucleon, e' is the scattered electron being detected, $\pi^{\pm}$ is the detected hadron (charged pion), and X is the final-state particles not being detected. The unpolarized SIDIS differential cross section is expressed as

$$\frac{d\sigma}{dx_{bj}dydz_h d\phi_S dP_t^2 d\phi_h} = \frac{\alpha^2}{2Q^2 x_{bj} y}\left[A F_{UU} + B F_{UU}^{\cos\phi_h}\cos\phi_h + C F_{UU}^{\cos 2\phi_h}\cos 2\phi_h\right], \tag{1}$$

where α is the electromagnetic fine-structure constant, $A = [1 + (1-y)^2]$, $B = 2(2-y)\sqrt{1-y}$, $C = 2(1-y)$, $x_{bj} = Q^2/(2P\cdot q)$, $y = (P\cdot q)/(P\cdot l)$, $z_h = (P\cdot P_h)/(P\cdot q)$, $q = l - l'$, and $Q^2 = -q^2$ [13,15–17]. The angle ϕ_S is the azimuthal angle of the nucleon spin direction, and can be integrated out in the unpolarized SIDIS process yielding an additional 2π factor for the F_{UU}. The reference frame and the definition of the azimuthal angle ϕ_h between the lepton scattering plane and the hadron plane follow the "Trento Conventions" as in Ref. [35]. The transverse momentum of the detected hadron is denoted as P_t.

The structure function F_{UU} involves a convolution of the unpolarized TMD PDF $f_q(x_{bj},k_\perp)$ and TMD FF $D_q(z_h,p_\perp)$, where $k_\perp$ is the intrinsic transverse momentum of the parton and $p_\perp$ is the transverse momentum of the fragmenting hadron with respect to the parton. The structure function $F_{UU}^{\cos\phi_h}$ at the lowest twist (twist-3), consists of a Cahn contribution and a Boer–Mulders contribution. The structure function $F_{UU}^{\cos 2\phi_h}$ consists of a twist-2 Boer–Mulders contribution and a twist-4 Cahn contribution. The Cahn contributions involve the convolution of the unpolarized TMD PDF $f_q(x_{bj},k_\perp)$ and TMD FF $D_q(z_h,p_\perp)$. The Boer–Mulders contributions involve the convolution of the Boer–Mulders TMD PDF $\Delta f_{q^\uparrow}(x_{bj},k_\perp) = -h_1^\perp(x_{bj},k_\perp)\cdot k_\perp/M_p$ and the Collins TMD FF $\Delta D_{q^\uparrow}(z_h,p_\perp) = 2p_\perp \cdot H_1^\perp(z_h,p_\perp)/(z_h M_h)$. A unit vector is defined for convenience as $\mathbf{h} \equiv \mathbf{P_t}/|\mathbf{P_t}|$. The structure functions are given below with the momentum conservation condition $\mathbf{P_t} = z_h\mathbf{k}_\perp + \mathbf{p}_\perp$:

$$F_{UU} = \sum_q e_q^2 x \int d^2\mathbf{k}_\perp f_q(x_{bj},k_\perp) D_q(z_h,p_\perp), \tag{2}$$

$$F_{UU}^{\cos\phi_h}\big|_{\text{Cahn}} = -2\sum_q e_q^2 x \int d^2\mathbf{k}_\perp \frac{\mathbf{k}_\perp\cdot\mathbf{h}}{Q} f_q(x_{bj},k_\perp) D_q(z_h,p_\perp), \tag{3}$$

$$F_{UU}^{\cos\phi_h}\big|_{\text{BM}} = \sum_q e_q^2 x \int d^2\mathbf{k}_\perp \frac{k_\perp}{Q}\frac{P_t - z_h\mathbf{k}_\perp\cdot\mathbf{h}}{p_\perp} \Delta f_{q^\uparrow}(x_{bj},k_\perp)\Delta D_{q^\uparrow}(z_h,p_\perp), \tag{4}$$

$$F_{UU}^{\cos 2\phi_h}\big|_{\text{BM}} = \sum_q e_q^2 x \int d^2\mathbf{k}_\perp \frac{P_t\mathbf{k}_\perp\cdot\mathbf{h} + z_h[k_\perp^2 - 2(\mathbf{k}_\perp\cdot\mathbf{h})^2]}{2k_\perp p_\perp} \Delta f_{q^\uparrow}(x_{bj},k_\perp)\Delta D_{q^\uparrow}(z_h,p_\perp), \tag{5}$$

$$F_{UU}^{\cos 2\phi_h}\big|_{\text{Cahn}} = 2\sum_q e_q^2 x \int d^2\mathbf{k}_\perp \frac{2(\mathbf{k}_\perp\cdot\mathbf{h})^2 - k_\perp^2}{Q^2} f_q(x_{bj},k_\perp) D_q(z_h,p_\perp). \tag{6}$$

Phenomenologically, the Gaussian ansatz is often utilized in TMD parametrizations. The unpolarized TMD PDF $f_q(x_{bj},k_\perp)$ and unpolarized TMD FF $D_q(z_h,p_\perp)$ are expressed as

$$f_q(x_{bj},k_\perp) = f_q^c(x_{bj})e^{-k_\perp^2/\langle k_\perp^2\rangle}/(\pi\langle k_\perp^2\rangle), \tag{7}$$

$$D_q(z_h,p_\perp) = D_q^c(z_h)e^{-p_\perp^2/\langle p_\perp^2\rangle}/(\pi\langle p_\perp^2\rangle), \tag{8}$$

where $f_q^c(x_{bj})$ is the collinear PDF, $D_q^c(z_h)$ is the collinear FF, $\langle k_\perp^2\rangle$ and $\langle p_\perp^2\rangle$ are the Gaussian widths as phenomenological parameters. In addition, the widths $\langle k_\perp^2\rangle$ and $\langle p_\perp^2\rangle$ in different studies have different forms of kinematical dependence: x_{bj} dependence for $\langle k_\perp^2\rangle$ and/or z_h dependence for $\langle p_\perp^2\rangle$ [15–17]. The knowledge about the flavor dependence of $\langle k_\perp^2\rangle$ and $\langle p_\perp^2\rangle$ is limited [36], and flavor independence has been assumed in most of the studies. The Boer–Mulders TMD PDF and Collins TMD FF are parametrized as in Ref. [15].

III. EXPERIMENT

The experiment E06-010, as introduced in Sec. I and in published studies of this experiment [29–32], produced data sets with a polarized 5.9 GeV electron beam and a transversely polarized ^{3}He gas target. The scattered electrons were recorded by the BigBite spectrometer [37–39] and the electroproduced pions ($\pi^\pm$) were recorded by the High Resolution Spectrometer (HRS) [40]. To study the unpolarized SIDIS processes, the data with opposite polarization states were combined. The charge difference between the two opposite beam polarizations for the entire experiment was less than 10 ppm [32]. The net ^{3}He polarization after the data combination is less than 0.5%.

In the experiment, the target system consisted of a 40-cm-long glass cell containing about 10 atm of ^{3}He gas polarized by the technique of spin-exchange optical pumping [41]. The direction of the ^{3}He polarization was flipped every 20 minutes. At each flip, the percentage of the ^{3}He polarization was measured and recorded. The temperature and density of the ^{3}He gas in the target cell was monitored and recorded in the data together with the information from the detectors.

The BigBite spectrometer was placed to the beam right facing the beam dump. The central polar angle of the BigBite was set at 30° in the laboratory frame. The angular acceptance of the BigBite was $(-140, 140)$ mrad for the in-plane angle and $(-240, 240)$ mrad for the out-of-plane angle. BigBite's polar and azimuthal angular acceptance ranges in the laboratory frame were 23° to 40° and 245° to 300°, respectively. The momentum acceptance range of BigBite was from 0.6 GeV to 2.5 GeV. A set of fiducial cuts were applied to the events in BigBite to suppress the edge effect associated with the acceptance. The fiducial cuts further reduced the acceptance of BigBite and are discussed in Sec. IV A.

The BigBite spectrometer consisted of a single dipole magnet, eighteen planes of multiwire drift chambers in three groups, and a scintillator plane between the lead-glass preshower and shower calorimeters. Knowledge of the magnetic field and the information from the drift chambers were used to reconstruct the tracks of charged particles. The trigger was formed by summing the signals from the preshower and shower calorimeters. The preshower and shower energy deposition with the reconstructed momentum were utilized for the particle identification (PID) in BigBite [37–39,42].

The HRS was placed to the beam left. In the laboratory frame, the central polar angle of the HRS was set at 16°. The angular acceptance range of the HRS was relatively small: $(-30, 30)$ mrad for the in-plane angle and $(-60, 60)$ mrad for the out-of-plane angle. In the laboratory frame, the polar and azimuthal angular acceptance ranges of the HRS were 13.5° to 18.5° and 78° to 102°, respectively. The momentum acceptance range of the HRS was set in the range $(1.0\% \pm 4.5\%) \times 2.35$ GeV. The fiducial cuts applied to the HRS are discussed in Sec. IV A.

The HRS was configured for hadron detection. The trigger was provided by two scintillator planes. Four detectors in the HRS were used for PID: a CO_2 gas Čerenkov detector for electron identification, an aerogel Čerenkov detector for pion identification, a ring imaging Čerenkov (RICH) detector for $\pi^\pm$, $K^\pm$, and proton identification, and two layers of lead-glass calorimeter for electron-hadron separation [40,42,43].

In this experiment, only one configuration was used. The beam energy, angle, and momentum settings of the BigBite spectrometer and the HRS were kept the same throughout the production runs. The experiment covered a kinematic range $0.12 < x_{bj} < 0.45, 1 < Q^2 < 4\,(\mathrm{GeV}/c)^2, 0.45 < z_h < 0.65$, and $0.05 < P_t < 0.55$ GeV/c in this configuration.

IV. DATA ANALYSIS

The data analysis for the unpolarized SIDIS differential cross section is more complicated than that for the asymmetry studies due to the need for a thorough understanding and description of the experimental acceptance as well as a good control of the systematic uncertainties, because some of which were less important due to the cancellation in the asymmetry studies. Dedicated developments and updates of the detector models in the simulation enabled a good description of the experimental acceptance, and have been successfully used in single electron channels as well as coincidence SIDIS channels. Detailed studies of the systematic uncertainties have been carried out thoroughly for the cross section extraction and the overall systematic uncertainty is mostly under 10%. In addition, radiative corrections, exclusive tail subtractions, and bin-centering corrections have been applied. In this section, the general procedures of the data analysis will be presented first. Then each element comprising the entire analysis will be discussed.

A. General procedures of data analysis

In each run of the experiment, the beam charge, the data-acquisition (DAQ) livetime, and the target temperature were recorded in the data together with the information on the detected particles from the detectors. The number of beam electrons was calculated from the recorded beam charge for each run. The target number density was calculated in each run based on the filling density of ^{3}He gas in the target, the target geometry and the target temperature values at different parts of the target cell.

Conventionally the data luminosity is defined as the product of the number of beam-electrons N_e, the target number density ρ_{tar}, and the target length l_{tar}. In each run, due to the DAQ livetime, the luminosity corresponding to the recorded data (effective data-luminosity) is the product of the conventional data luminosity and the DAQ livetime f_{live}. To include the livetime correction in the data normalization procedure, we defined the effective data luminosity L_{d} as in the following expression:

$$L_{\text{d}} = N_e f_{\text{live}} \rho_{\text{tar}} l_{\text{tar}}. \tag{9}$$

The individual runs were combined together in the analysis and the effective data luminosity related to each of the combined runs were summed to normalize the data when extracting the differential cross sections.

The beam current was measured by the beam current monitors (BCMs) in Hall A [40]. The beam current was calculated by using the signal from the two rf cavities of the BCMs in this experiment. The rf cavities were calibrated by the "OLO2" cavity which measured the beam current at the injector [42]. The beam charge was from the integration of the beam current and had a precision at the level of 1%.

The overall detection efficiencies of the detectors were also included in the normalization of the data. The use of the elastic electron-proton (*ep*) calibration runs and the inclusive DIS channel to determine these overall efficiencies is discussed in Secs. IV B and IV C.

The study of the experimental acceptance was the most difficult part of the data analysis. Several fiducial kinematic cuts on the electron and hadrons were applied in addition to the general tracking-quality cuts and the PID cuts. Details of the general tracking-quality cuts can be found in the published studies of this experiment [29–32] and the theses [42,44]. The fiducial kinematic cuts were applied to suppress the systematic uncertainties related to the description of the experimental acceptance by using the Monte Carlo (MC) simulation. These cuts were varied around the central values when estimating the systematic uncertainties.

For the electron events recorded by the BigBite spectrometer, the momentum cuts were $0.9 < P_e < 2.5$ GeV. In addition to the consideration of acceptance, the high value of 0.9 GeV was set to suppress the large systematic uncertainties in the low-momentum range. The dominant systematic uncertainties in the low-momentum range came from two sources. They are the drifts of the total-shower-energy threshold for the BigBite trigger during the experiment and the photon-induced electron contamination, which will be discussed in Sec. IV D.

The fiducial cuts on the angles for the electron events were $25^\circ < \theta_e < 37^\circ$ and $250^\circ < \phi_e < 295^\circ$.

The fiducial momentum cuts for the $\pi^\pm$ events in the HRS were $2.26 < P_{\text{hrs}} < 2.41$ GeV. The fiducial angular cuts for the $\pi^\pm$ events were $14^\circ < \theta_{\text{hrs}} < 18^\circ$ and $81^\circ < \phi_{\text{hrs}} < 99^\circ$.

Several cuts were applied to select the SIDIS events: four-momentum-transfer squared $Q^2 > 1$ GeV^2, invariant mass $W > 2.3$ GeV, and the mass of undetected final-state particles $W' > 1.6$ GeV, assuming scattering on a nucleon.

The in-plane and the out-of-plane angular acceptance range of the HRS with the fiducial cuts were (−26, 26) mrad and (−45, 45) mrad, respectively. The in-plane and the out-of-plane angular acceptance range of BigBite with the fiducial cuts were (−90, 100) mrad and (−200, 180) mrad, respectively. The relatively large angular acceptance range of the scattered electrons detected by BigBite provided a relatively large angular acceptance range of the virtual photon $\vec{q}$. The range of the ϕ_h angle was much larger than the angular acceptance of the HRS because it is defined with respect to $\vec{q}$. The ranges of kinematic variables ϕ_h, x_{bj}, z_h, Q^2 and P_t from the data with the fiducial cuts, the PID cuts, and the SIDIS-event-selection cuts can be seen in Sec. IV E where the kinematical correlations of these variables are presented. The range of ϕ_h allowed up to 10 bins to examine the ϕ_h dependence of the SIDIS differential cross sections.

There was a small amount of N_2 gas with known density in the ^{3}He target cell. The backgrounds from the N_2 gas were subtracted by using the N_2 reference cell runs taken with N_2-filled target. A proper scaling was applied based on the effective luminosity ratios between these runs and the ^{3}He production runs.

B. Monte Carlo simulations

For a full description of the experimental acceptance of E06-010, a model for the BigBite spectrometer used in E06-010 for electron detection has been developed and incorporated into the SIMC package [45] which was initially developed for JLab Hall C experiments and used for the semi-inclusive studies in Hall C [22]. It was adapted for this experiment [46]. It contains a realistic description of various detectors including the HRS used in the experiment E06-010 for hadron detection. The energy-loss, multiscattering, and pion decay processes have also been included in the SIMC package. The radiation length and materials in the simulation were defined based on the configuration of experiment E06-010.

The external radiative effects included the energy loss and multiscattering for the particles before and after scattering and were included in the analysis relying on the SIMC package. The internal radiative effects are more closely related to the change of the Born cross sections, including the vacuum polarization, vertex correction, and contributions from higher-order Feynman diagrams. The internal radiative effects were evaluated by using additional packages based on the process being studied.

The BigBite detector model was tested by using the calibration runs of elastic *ep* scattering at incident electron beam energies of 1.23 and 2.4 GeV (Fig. 1), as well as the inclusive DIS channel from the ^{3}He production data at 5.9 GeV (Fig. 2) by using the singles trigger of BigBite. The inclusive DIS data from the H_2 reference cell runs and the ^{3}He production runs at 5.9 GeV with the singles trigger of the HRS have been used to test the description of the HRS experimental acceptance (Figs. 3 and 4).

In the simulation of elastic *ep* scattering, the form factors from Ref. [47] were used. The internal radiative effects were based on Ref. [48]. The results from the simulation used the same luminosity values as the total effective data luminosity of the combined data. In the simulations, only the elastic *ep* process was included, thus only the invariant mass W peak of the proton was observed in both the simulation and the data while the peaks from higher resonances are only observed

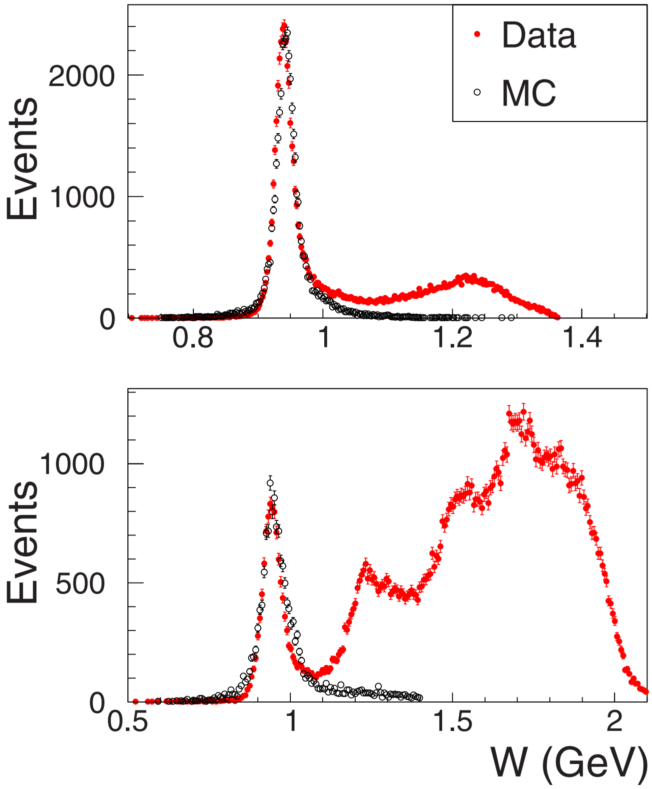

FIG. 1. The invariant mass W comparisons between data and simulation (MC) for 1.23 GeV (top panel) and 2.4 GeV (bottom panel) beam elastic *ep* calibration run using BigBite. The error bars represent the statistical uncertainties. The red solid circles are from the data. The black open circles are from the simulation.

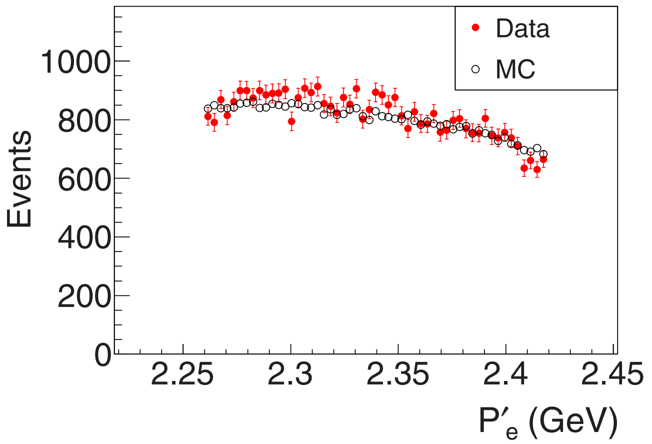

FIG. 3. The scattered electron momentum (P_e') comparison of the H_2 inclusive DIS channel in the HRS between the data and the simulation (MC). The error bars represent statistical uncertainties. The red solid circles are from the data. The black open circles are from the simulation.

in the data. In both panels of Fig. 1, the numbers of events from the simulation were scaled with an overall factor of 73% to obtain the agreement on the proton W peaks between the simulation and the data. This factor was used as the overall detection efficiency of electron events in the BigBite spectrometer. The elastic *ep* data were under the same general tracking-quality cuts, electron PID cuts, and angular fiducial cuts as used for the electron events in inclusive DIS and SIDIS. The same kinematic cuts were applied to the simulation. The same binning was used for the comparisons between the data and the simulation. Good agreements between the data and the simulation for the proton W peaks are observed in Fig. 1.

The HRS with the setting for the production runs could not access the elastic *ep* scattering, because the scattered electrons were outside the acceptance range of the HRS. To test the acceptance description for the HRS, the inclusive DIS data from the H_2 reference cell runs and the ^{3}He production runs at 5.9 GeV beam energy were used. The structure functions for the inclusive DIS channels were taken from a widely used model [49]. The model provided a good description of the

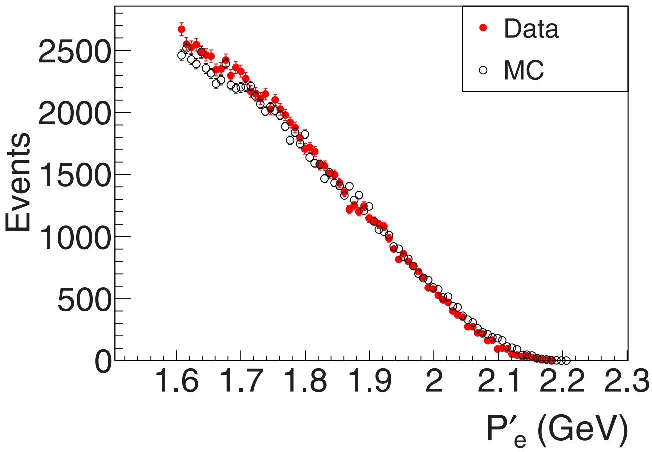

FIG. 2. The scattered electron momentum (P_e') comparison of the ^{3}He inclusive DIS channel in BigBite between the data and the simulation (MC). The error bars represent statistical uncertainties. The red solid circles are from the data. The black open circles are from the simulation.

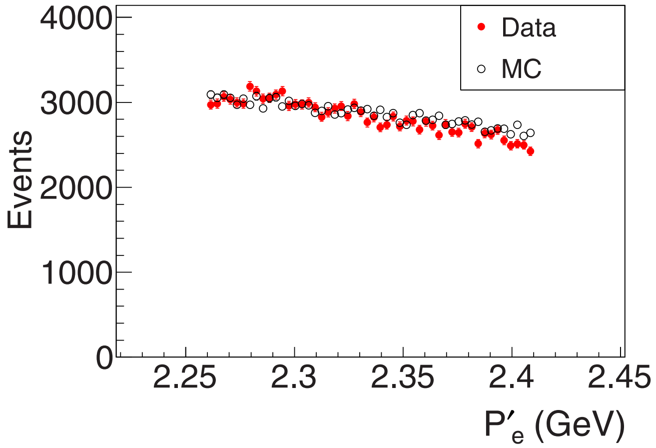

FIG. 4. The scattered electron momentum (P_e') comparison of the ^{3}He inclusive DIS channel in the HRS between the data and the simulation (MC). The error bars represent statistical uncertainties. The red solid circles are from the data. The black open circles are from the simulation.

unpolarized inclusive DIS cross sections for the ^{3}He target in experiment E06-014 [50,51] which had a similar kinematic range.

In the kinematic range of the HRS, the contribution from the quasi-elastic radiative tail was estimated to be negligible using the simulations. The photon-induced electron contamination was estimated to be negligible by comparing the electron and positron yields in the HRS with negative and positive polarities. The difference introduced by using different methods for internal radiative effects (Mo and Tsai [52] and POLRAD [53]) was less than 1%. An overall scaling factor of 100% was used in the simulations in Figs. 3 and 4. This overall efficiency at 100% is close to what was found in experiment E06-014 (99.95%) [50]. The N_2 background in the ^{3}He runs were subtracted by using the N_2 runs. The efficiency of the PID cuts (PID-cut efficiency) and the remaining contamination from negatively charged hadrons and the photon-induced electron after the PID cuts were corrected for by using the expression below:

$$N_{\rm corr} = N(1 - f_{\rm contam})/f_{\rm eff}({\rm PID}), \tag{10}$$

where $f_{\rm eff}$(PID) is the PID-cut efficiency and $f_{\rm contam}$ is the fraction of the remaining contamination. The PID-cut efficiency $f_{\rm eff}({\rm PID}) = N_1/N_0$ is the ratio of the number of good events after the PID cuts (N_1) over the number of good events before the PID cuts (N_0). The fraction of the contamination $f_{\rm contam} = N_{\rm contam}/N$ is the ratio of the number of events from the contamination $N_{\rm contam}$ over the total number of events N after the PID cuts. After the PID cuts, the total number of events consisted of the good events and the contamination events ($N = N_{\rm contam} + N_1$). The methods to determine the ratios $f_{\rm eff}$(PID) and $f_{\rm contam}$ have been well established in the previous studies of this experiment [29–32,42–44].

In Figs. 3 and 4, the fiducial kinematic cuts on the HRS and the cuts selecting the DIS events ($Q^2 > 1$ GeV^2 and $W > 2.3$ GeV) were applied. Agreements between the data and the simulation are observed.

In the kinematic range $P_e > 1.6$ GeV of the BigBite spectrometer, the contribution from the quasi-elastic radiative tail and the photon-induced electron contamination were less than 2%, but both increased to large values in lower momentum ranges. This has been observed in experiment E06-014 [50,51] as well. The determination of the photon-induced electron contamination was done by comparing the positron yield in BigBite with the reversed magnetic field and the electron yield in the production runs. In experiment E06-010, the photon-induced electron contamination involved larger uncertainties in the inclusive channel than in the semi-inclusive coincidence channel, as the runs for subtracting this contamination provided limited statistics for the inclusive channel (due to large prescale factors) while providing high statistics for the semi-inclusive channels. In addition, we also found different methods for internal radiative effects (Mo and Tsai [52] and POLRAD [53]) and different models for the quasi-elastic cross sections (from Refs. [49,54]) gave quite different estimations for the quasi-elastic radiative tails in the range $P_e < 1.6$ GeV. The estimation for the fraction of events from the quasi-elastic tail could differ up to ∼10% around $P_e = 1.0$ GeV, while the differences were less than 1% in the range $P_e > 1.6$ GeV.

Considering the complications above for the inclusive DIS channel in the kinematic range $P_e < 1.6$ GeV in BigBite, we only present the comparison of the data and the simulation in the range $P_e > 1.6$ GeV in Fig. 2 as an additional test for the acceptance description of BigBite besides the elastic *ep* channels. The same general tracking-quality cuts, the electron PID cuts, and all the fiducial cuts on the electron side were applied to the data. The same cuts on the kinematic variables in addition to the fiducial cuts were applied to the data and the simulation to select the DIS events; namely, $Q^2 > 1$ GeV^2 and $W > 2.3$ GeV. The same overall scaling factor (73%) as in the elastic *ep* simulations was used to obtain the agreement between the data and the simulation. The subtraction of the N_2 background and the corrections for the PID-cut efficiency and the contamination were carried out in the same way as in the HRS case. Agreements between the data and the simulation are observed.

All the production runs of the experiment were combined in the comparison between the data and the simulation for the ^{3}He inclusive DIS channel. We found that the overall detection efficiency combining all the production runs was about 100% for the HRS and about 73% for BigBite (consistent with the value found in the elastic *ep* channel). These overall detection efficiencies were used in the data normalization procedure in Sec. IV C.

C. Data corrections and cross-section extraction

A number of corrections needed to be applied to the data in order to extract the differential cross sections; namely, for the efficiency, contamination and background subtraction and the acceptance. To compare the experimental results with the theoretical and phenomenological models, the radiative corrections and the bin-centering corrections need to be applied in addition. The differential cross section from the data in a specific bin before the radiative corrections and the bin-centering corrections is denoted $\langle d\sigma/d{\rm PHS}\rangle_{\rm data}$ and can be expressed as follows:

$$\left\langle \frac{d\sigma}{d{\rm PHS}} \right\rangle_{\rm data} = N_{\rm data} f_{\rm corr} \frac{1}{L_{\rm d}} \frac{L_{\rm s}}{N_{\rm phs}}, \tag{11}$$

where $N_{\rm data}$ is the number of events from the data in this bin, $f_{\rm corr}$ is the factor for the data corrections, $L_{\rm d}$ is the effective data luminosity, $L_{\rm s}$ is the phase-space simulation luminosity, and $N_{\rm phs}$ the number of events from the phase-space simulation in this bin. In this paper, the differential phase space $d{\rm PHS} = dx_{bj}dydz_hd\phi_S dP_t^2 d\phi_h$ is used for the results.

The data-correction factor $f_{\rm corr}$ included the correction for the efficiency and the contamination and background and can be expressed as

$$f_{\rm corr} = \left[1 - \sum_i f_{\rm contam}(i)\right] \prod_j \frac{1}{f_{\rm eff}(j)}, \tag{12}$$

where $f_{\rm contam}(i)$ is the contamination fraction of the ith type and $f_{\rm eff}(j)$ is the efficiency of the jth type. The fraction $f_{\rm contam}(i)$ was defined as the ratio of the number of events from the ith type of contamination and background over the total number of events.

The types of contamination and background included the events from the radiative tails of the exclusive channels, the N_2 background, and the remaining contaminations after the PID cuts.

The types of efficiencies included the PID-cut efficiencies and the overall detection efficiencies of BigBite and the HRS. The correction for the $\pi^{\pm}$ decay was included in Eq. (12) as f_{eff}(decay) which was evaluated for each bin as in Eq. (21).

The acceptance corrections were included in the method of using the phase-space simulation to convert the numbers of events to differential cross sections. This method requires a good description of the acceptance of BigBite and the HRS, which were checked by using the elastic *ep* scattering and the inclusive DIS channels as in Sec. IV B. The acceptance corrections were based on the Monte Carlo simulation with the same kinematic cuts as applied to the data. The number of events in each bin from the simulation weighted by the theoretical cross section (N_{sim}) divided by the phase-space (nonweighted) simulation with the same kinematic cuts in the same bin (N_{phs}) becomes the (averaged) theoretical cross section in this bin. The same was done for the data events N_{data}, forming a quantity $(N_{\text{data}}/N_{\text{phs}})(L_{\text{s}}/L_{\text{d}})$ in each bin from which the experimental cross section can be determined. The luminosities (L_{d} and L_{s}) were used to normalize the numbers of events, both for the data (N_{data}) and the simulation (N_{phs}). The numbers of events in a specific bin of data, weighted and phase-space (nonweighted) simulations are expressed as

$$N_{\text{data}} = \left\langle \frac{d\sigma}{d\text{PHS}} \right\rangle_{\text{data}} \Delta\text{PHS}_{\text{d}} f_{\text{acc,d}} L_{\text{d}}, \tag{13}$$

$$N_{\text{sim}} = \left\langle \frac{d\sigma}{d\text{PHS}} \right\rangle_{\text{sim}} \Delta\text{PHS}_{\text{s}} f_{\text{acc,s}} L_{\text{s}}, \tag{14}$$

$$N_{\text{phs}} = 1 \Delta\text{PHS}_{\text{s}} f_{\text{acc,s}} L_{\text{s}}, \tag{15}$$

where $\Delta\text{PHS}_{\text{d}}$ is the phase space in the data for a specific bin, and $\Delta\text{PHS}_{\text{s}}$ is the phase space in the simulations. The factor $f_{\text{acc,d}}$ represents the acceptance effect in the data, and $f_{\text{acc,s}}$ represents the acceptance effect in the simulations. The factor L_{d} is the total effective data luminosity, and L_{s} is the luminosity in the simulations. The quantities ΔPHS_i and $f_{\text{acc},i}$ are related to the acceptance, the fiducial and kinematic cuts and the boundaries of the specific bin, where $i = \text{d (s)}$ represents the quantities in the experiment (simulation).

The description of experimental acceptance has been tested by using known channels as in Sec. IV B. The tested framework of simulation provided agreement between $\Delta\text{PHS}_{\text{s}} f_{\text{acc,s}}$ and $\Delta\text{PHS}_{\text{d}} f_{\text{acc,d}}$ with less than 10% uncertainties.

A cut on the total shower energy was applied to the data and the simulations in addition to the fiducial cuts due to the complicated and time-dependent drifts of the total shower energy threshold for the BigBite trigger during the experiment. To address this issue, a total shower energy cut of $E_{\text{tot}} > 900$ MeV was used, high enough to override the fluctuations of threshold-related inefficiency, but not too high to significantly reduce the kinematic range and the valuable data. A description of the total shower energy deposition was developed and included in the BigBite model of simulation, based on the experimental data from the BigBite calibration runs and checked by the production runs. The correction for the efficiency of this cut was included in the ratio $N_{\text{data}}/N_{\text{phs}}$ in which the numbers of events from the data (N_{data}) and from the phase-space simulation (N_{phs}) were obtained with the same E_{tot} cut and kinematic cuts.

The radiative corrections (RCs) were applied to the differential cross sections of the data in addition to the data corrections in Eq. (11). The radiative corrections were based on the ratios of the weighted simulations with and without radiative effects. The external radiative effects were included by using the SIMC package as illustrated in Sec. IV B. The internal radiative effects were included by using the HAPRAD package [55]. The internal radiative effects based on Mo and Tsai [52] built in SIMC were used as a comparison and to estimate systematic uncertainties, as in Ref. [22].

The numbers of events in a specific bin of weighted simulations with and without radiative effects ($N_{\text{sim}}^{\text{rad}}$ and $N_{\text{sim}}^{\text{nr}}$) are expressed as below:

$$N_{\text{sim}}^{\text{rad}} = \left\langle \frac{d\sigma}{d\text{PHS}} \right\rangle_{\text{sim,rad}} \Delta\text{PHS}_{\text{s}} f_{\text{acc,s}} L_{\text{s}}, \tag{16}$$

$$N_{\text{sim}}^{\text{nr}} = \left\langle \frac{d\sigma}{d\text{PHS}} \right\rangle_{\text{sim,nr}} \Delta\text{PHS}_{\text{s}} f_{\text{acc,s}} L_{\text{s}}, \tag{17}$$

where $\Delta\text{PHS}_{\text{s}}$ is the phase space in the simulations for this specific bin, $f_{\text{acc,s}}$ is the acceptance factor in the simulations, and L_{s} is the luminosity in the simulations.

In the simulations, each generated event had its own kinematics. Before the scattering the energy and direction of the electron were set according to the beam configuration, the target particle was fixed. When the external radiative effects were turned on, the electron went through materials and had a certain energy loss and direction change. After the scattering, the scattered electron and electroproduced hadron went through materials and experienced certain amounts of energy loss and direction change. Thus, when the external radiative effects were turned on, an event had two sets of kinematics, one set at the interaction point was for weighting-factor calculation and the other set that went to the detector models determined whether this event was accepted. When the external radiative effects were turned off, the two sets of kinematics were the same.

A value of differential cross section ($d\sigma/d\text{PHS}$) was calculated for each event as the weighting factor using its kinematics at the interaction point. For the simulation without radiative effects, $d\sigma/d\text{PHS}$ was the Born differential cross section. For the simulation with radiative effects, $d\sigma/d\text{PHS}$ was the internally radiated differential cross section by using the HAPRAD package [55] on top of the Born differential cross section. A Monte Carlo simulation using a uniform sampling in the phase space $d\text{PHS}$ gave a numerical integration of the weighting factor $d\sigma/d\text{PHS}$ in a defined total phase space $\Delta\text{PHS}_{\text{s}}$.

In this study, when generating the events in the simulations, a phase space larger than (and containing) the acceptance range was used. Due to the acceptance effect, not all the generated events could pass through the detector models and be accepted.

When a specific bin was under study, only the events with kinematics within the boundaries of the bin were selected. The combined effect from the acceptance, the bin boundaries, and the kinematic cuts is symbolized as the factor $f_{\mathrm{acc,s}}$ in Eqs. (16) and (17).

The averaged differential cross sections from the simulations with and without radiative effects in a specific bin are denoted as $\langle d\sigma/d\mathrm{PHS}\rangle(\mathrm{sim,rad})$ and $\langle d\sigma/d\mathrm{PHS}\rangle(\mathrm{sim,nr})$, respectively. The number of events in a specific bin is proportional to the averaged differential cross sections. The ratio $C_{\mathrm{rc}} = N^{\mathrm{rad}}_{\mathrm{sim}}/N^{\mathrm{nr}}_{\mathrm{sim}}$ is used as the radiative correction coefficient for this specific bin.

Different models for the Born differential cross section would result in different C_{rc}, and the proper coefficients C_{rc} can be determined when the simulation with radiative effects match the data [after the corrections in Eq. (12)]. The matching was found by tuning certain parameters in a certain phenomenological model until the difference between the data and the simulation in each bin was close to or less than the corresponding total experimental uncertainty. Then in each bin, the coefficient C_{rc} was applied to the differential cross section from the data [right-hand side of Eq. (11)] as

$$\sigma^{\mathrm{bin}}_{\mathrm{expt}} = \frac{1}{C_{\mathrm{rc}}}\left\langle \frac{d\sigma}{d\mathrm{PHS}}\right\rangle_{\mathrm{data}}, \tag{18}$$

where $\sigma^{\mathrm{bin}}_{\mathrm{expt}}$ represents the differential cross section extracted experimentally after the RCs.

The bin-centering corrections (BCCs) were evaluated in each bin. The need for the BCCs and the calculation are presented in the following paragraphs. The values of kinematic variables in a bin were determined by averaging the experimental data. For example, the value of a variable x in a certain bin was determined by

$$\overline{x} = \frac{1}{N_{\mathrm{data}}}\sum x_i, \tag{19}$$

where $\overline{x}$ is the averaged value of x, N_{data} is the total number of events in this bin and x_i is the x value of the ith event. The symbol x stands for any kinematic variable. The averaged values of the kinematic variables (x_{bj}, z_h, Q^2, ϕ_h, and P_t) from the simulation were consistent with the data mostly within 0.5%.

The differential cross section extracted from the data in a specific bin ($\sigma^{\mathrm{bin}}_{\mathrm{expt}}$) using Eqs. (11) and (18) was an averaged value and can be directly compared with the averaged differential cross section $\sigma^{\mathrm{bin}}_{\mathrm{MC}}$ from the simulation in the same bin.

The averaged differential cross section $\sigma^{\mathrm{bin}}_{\mathrm{MC}} = \overline{\sigma}_{\mathrm{model}}$ was not necessarily equal to $\sigma_{\mathrm{theory}} = \sigma_{\mathrm{model}}(\overline{\mathrm{vars}})$, where $\sigma_{\mathrm{model}}(\mathrm{vars})$ is the theoretical model for the differential cross sections, the symbol vars represents the collection of kinematic variables (x_{bj}, z_h, Q^2, ϕ_h, and P_t) and $\overline{\mathrm{vars}}$ represents the averaged values of kinematic variables in this bin ($\overline{x_{bj}}$, $\overline{z_h}$, $\overline{Q^2}$, $\overline{\phi_h}$, and $\overline{P_t}$). For the purpose to compare theoretical model σ_{theory} with the data, the ratio $\sigma_{\mathrm{theory}}/\sigma^{\mathrm{bin}}_{\mathrm{MC}}$ was applied to the data in each bin, based on the same tuned model of Born differential cross section as used in the radiative corrections.

The BCC for the data in one bin is defined as

$$\sigma^{\mathrm{BCC}}_{\mathrm{expt}} = \frac{\sigma^{\mathrm{bin}}_{\mathrm{expt}}}{\sigma^{\mathrm{bin}}_{\mathrm{MC}}}\sigma_{\mathrm{theory}}, \tag{20}$$

where $\sigma^{\mathrm{BCC}}_{\mathrm{expt}}$ is the SIDIS differential cross section extracted experimentally, after the bin-centering correction with experimental central values of kinematic variables, and can be compared with the differential cross section in models evaluated at the same central values of kinematic variables.

A phenomenological model with a set of tuned parameters was used for the RCs and BCCs. The parameters were tuned in an iterative process. The comparisons of the Born differential cross section from this model and from the data with all the corrections are shown in Sec. V A. Using the model with parameters from the multidimensional fitting in Sec. V E changed the RCs and BCCs by less than 1% in all the bins.

The contribution from the exclusive channels $e + p \to e' + \pi^+ + n$ and $e + n \to e' + \pi^- + p$ were evaluated by using simulations with cross-section models tested in the kinematic range of this experiment [22]. The contributions from the exclusive channels were from 2% to 7.5% in the π^+ production channel and 0.5% to 3% in the π^- production channel.

The contribution of the $\pi^\pm$ from the decay of the gluon-exchange-produced ρ (diffractive ρ) is not a part of the SIDIS process and should be subtracted. The contribution of the $\pi^\pm$ from the decay of quark-exchange-produced ρ is part of the SIDIS process and should not be subtracted. We have simulated the contribution of the $\pi^\pm$ from the decay of the ρ, in the same way as in Ref. [22]. The model for the exclusive production of ρ was from PYTHIA [56] and was further tuned according to the ρ^0 cross section from a CLAS experiment at JLab as described in Ref. [22]. Comparing this simulation with the data, it was found that the fraction of the events from the ρ decay was mostly less than 5% in experiment E06-010. While the level of 5% was not completely negligible, the contribution from the decay of the diffractive ρ was considered to be negligible considering a recent study from CLAS [57]. In Ref. [57], the quark-exchange production of ρ was found to be dominant while the diffractive ρ from the gluon-exchange was found to be negligible. The fraction of the events from the decay of diffractive ρ was expected to be much smaller than 5% in the kinematic range $0.45 < z_h < 0.65$ of this experiment, thus at a negligible level.

In the experiment, the $\mu^\pm$ from the decay of a $\pi^\pm$ could not be discriminated from the $\pi^\pm$ in the HRS and was assumed to be a $\pi^\pm$ event. When a $\pi^\pm$ event decays to a $\mu^\pm$ and a neutrino, the kinematics of this event is changed. This effect was evaluated by using simulations. The SIMC package has an established component simulating the probability of the decay and the kinematic change of each $\pi^\pm$ event. The probability of the decay was calculated based on the length of the track of an event and the $\pi^\pm$ lifetime. The kinematic change was evaluated by generating the momentum and angles of the $\mu^\pm$ in the center-of-mass frame of the decaying $\pi^\pm$, from which the kinematics of the $\mu^\pm$ in the laboratory frame were calculated. In the center-of-mass frame of the decaying $\pi^\pm$, the momentum of the $\mu^\pm$ followed the four-momentum

TABLE I. Systematic uncertainties.

Source	Range (%)
e^- identification in BigBite	2.0–8.0
e^- overall detection efficiency in BigBite	<3.0
$\pi^\pm$ identification in the HRS	<2.0
Experimental acceptance corrections	5.0–10.0
Radiative corrections	1.0–3.5
Exclusive tail subtractions	1.0–3.0
Bin-centering corrections	<3.0

conservation and the angles were generated with a uniform probability distribution in the solid angle. The $\mu^\pm$ was recorded as a $\pi^\pm$ if it was in the acceptance of the HRS model, and was rejected otherwise.

The effect of the decay of $\pi^\pm$ was treated as one of the efficiency factor as

$$f_{\rm eff}(\text{decay}) = N_{\rm sim}(\text{decay})/N_{\rm sim}(\text{no decay}), \qquad (21)$$

where $N_{\rm sim}$(decay) and $N_{\rm sim}$(no decay) are the numbers of events recorded in the simulation with decay effect turned on and off, respectively.

The N_2 background in the SIDIS processes were evaluated using the N_2 reference runs. The N_2 background was around 10% depending on the kinematics.

The PID of electrons in BigBite was based on the combination of a cut in the preshower energy deposition and a 2D cut in the ratio of total-shower-energy deposition and the reconstructed momentum in order to suppress the π^- contamination. The PID cuts were optimized to maximize the PID-cut efficiency and minimize the π^- contamination. The fractions of the remaining π^- contamination and the PID-cut efficiencies were estimated based on fitting and discriminating the π^- and electron spectra in the preshower calorimeter. The PID-cut efficiencies increased from 70% to 98% and the fractions of the remaining π^- contamination decreased from 6% to less than 0.1%, in increasing momentum range of BigBite.

TABLE II. The central values of the kinematic variables in the pseudo-1D bins. The unit for Q^2 is GeV^2. The unit for P_t is GeV. The unit for ϕ_h is rad. The kinematic variables x_{bj}, y, and z_h have no unit.

x_{bj}	Q^2/GeV^2	z_h	ϕ_h/rad	P_t/GeV
0.163	1.47	0.476	3.10	0.437
0.188	1.70	0.484	3.08	0.411
0.208	1.85	0.491	3.07	0.392
0.228	2.00	0.499	3.07	0.371
0.249	2.14	0.508	3.06	0.350
0.272	2.29	0.519	3.06	0.325
0.297	2.45	0.530	3.05	0.299
0.325	2.62	0.543	3.05	0.271
0.358	2.81	0.557	3.04	0.239
0.393	3.09	0.562	3.02	0.216

A more significant contamination in the electron events was the photon-induced electrons from the pair-production. The π^0 meson, from the electroproduction, decays into two photons. The high-energy photons create the photon-induced electron contamination through the pair-production process. The percentage of this contamination in the total electron events was determined by comparing the positron yield in BigBite with the reversed magnetic field and the electron yield in the production runs. The photon-induced electron contamination increased from <1% to 40% when the electron

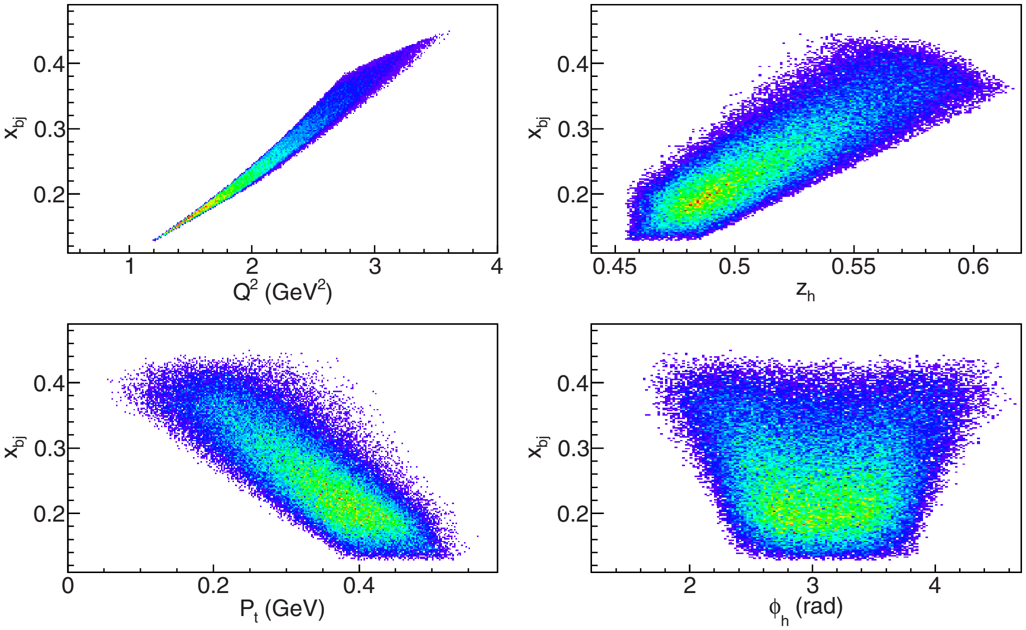

FIG. 5. The correlations between x_{bj} and other kinematic variables in experiment E06-010.

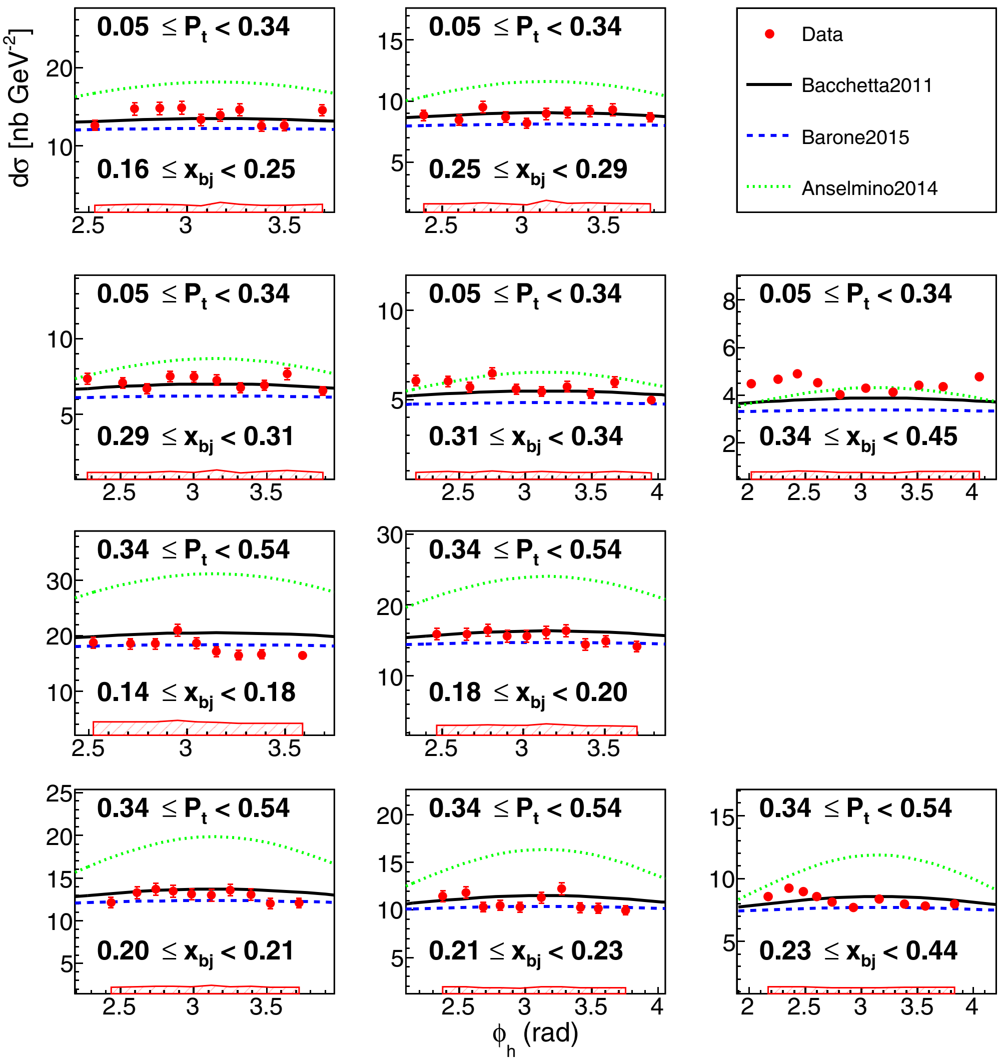

FIG. 6. The differential cross sections in 3D bins: the π^+ SIDIS production channel. The red circles are from the data, the black solid lines are from the model [17], the blue dashed lines are from the model [15], and the green dotted lines are from the model [16]. The error bars represent the statistical uncertainties of the data. The error band on the bottom of each panel represents the experimental systematic uncertainty. The P_t (in unit of GeV) and x_{bj} ranges of each plot are presented at the top and the bottom of the panel, respectively.

momentum range of BigBite decreased from >1.6 GeV to 0.7 GeV.

The PID of $\pi^\pm$ in the HRS was based on the combination of the gas Čerenkov, the aerogel Čerenkov, and the lead-glass calorimeter signals. The PID-cut efficiency and the contamination after the PID cuts have been evaluated and included in the correction. The contamination to the π^- events (<0.5%) came from the negatively charged non-pion hadron and electron. The contamination to the π^+ events (<1%) predominantly came from the positively charged non-pion hadron. The PID-cut efficiency for $\pi^\pm$ in the HRS was around 95%.

The overall detection efficiency of BigBite was evaluated by using the elastic *ep* scattering as in Sec. IV B. Two beam energies, 1.23 and 2.4 GeV, were used in the elastic *ep* runs, covering the low- and high-momentum acceptance of the BigBite spectrometer. The overall efficiency was also checked by using the inclusive DIS channel in the ^{3}He production data in a broad momentum range. The overall efficiency was estimated to be 73% to 75%. The overall efficiency of the HRS was estimated to be close to 100%, as in Sec. IV B.

D. Systematic uncertainties

The systematic uncertainties related to electron detection in BigBite were dominated by the photon-induced electron contamination and the efficiency of the total-shower-energy cut which was applied to remove the effect from the drift in the calorimeter threshold.

The photon-induced electron contamination was determined by the ratio of the positron yield and electron yield in each bin. The positron yield was from the runs with reversed magnetic field of BigBite. The electron yield was from the production runs. The acceptance of the positrons in the runs with reversed magnetic field of BigBite was the same as the acceptance of electrons in the production runs. The uncertainty in determining the positron yield was large in the low-momentum range of BigBite due to the large

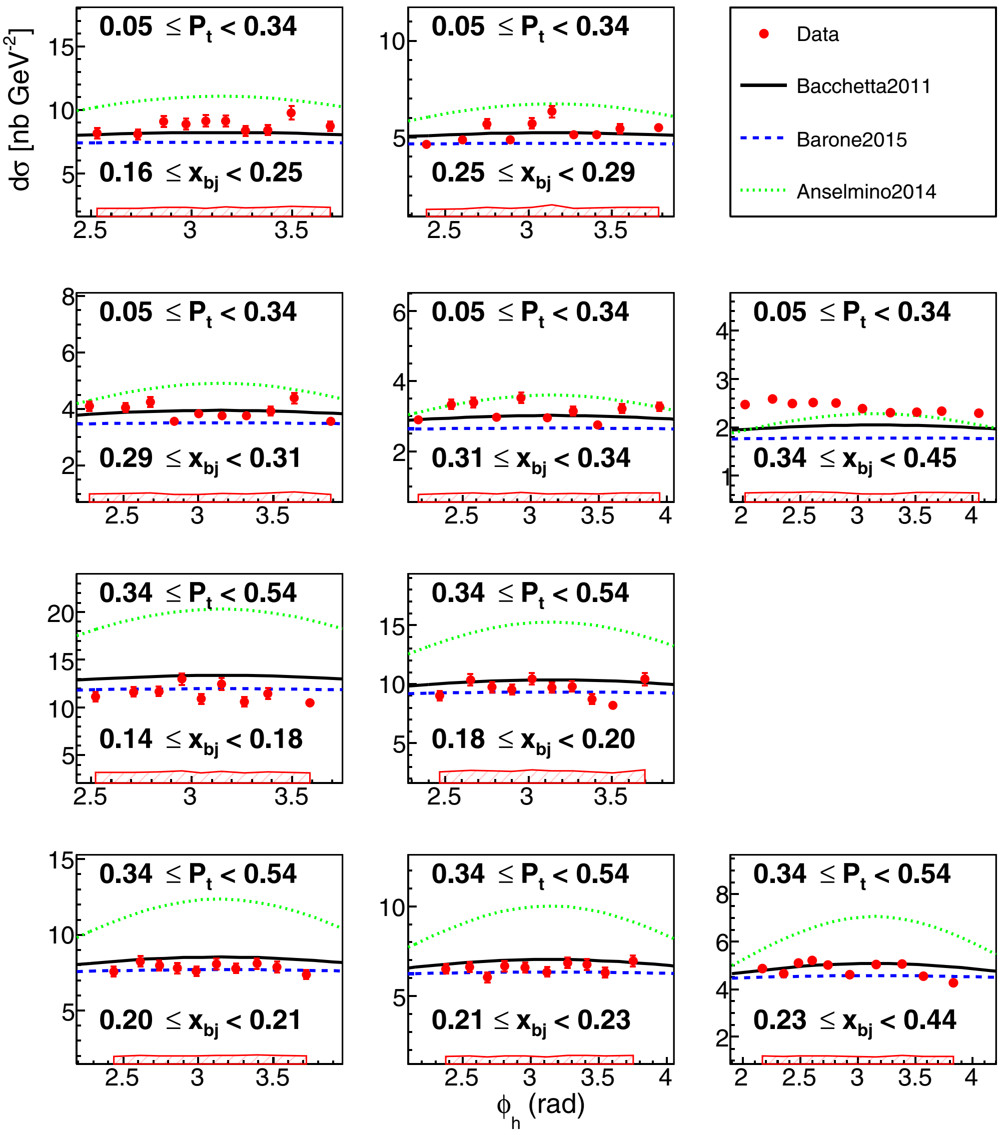

FIG. 7. The differential cross sections in 3D bins: the π^- SIDIS production channel. The definitions of the markers, the lines, and the bands are the same as Fig. 6 for the π^+ channel.

uncertainties from the PID-cut efficiency for the positrons and the large uncertainties from the π^+ contamination. The large π^+ contamination (up to 50% in the range of $P_e < 1$ GeV) made the process of fitting and discriminating the π^+ and positron spectra much more difficult than the process for the π^- and electron spectra in the production runs.

The events with a lower electron momentum deposited a lower total-shower energy and were more strongly affected by the total-shower-energy cut. Using the simulation to correct for the efficiency of the total-shower-energy cut involved increasing uncertainties in a decreasing momentum range of BigBite.

To evaluate the systematic uncertainties above, the PID cuts and the total-shower-energy cut have been varied (varied cut sets) around the central values (central cut set). In each bin, the number of events from the data and data corrections were found with each set of cuts. The data corrections were applied as in Eq. (11). The root-mean-square value of the differences of the results with the varied cut sets and with the central cut set has been used to define the systematic uncertainty.

The total systematic uncertainties related to the electron detection in BigBite are in the range from 3% to 10% depending on the kinematics.

The systematic uncertainties of the PID of $\pi^\pm$ events in the HRS were determined to be less than 2% by using the well-established techniques in the previous studies of this experiment [29–32,42,43].

In the coincidence channel for SIDIS, the systematic uncertainties in the experimental acceptance corrections by the simulation were determined by putting a series of kinematic cuts besides the central optimized set to both the data and the simulation. The total systematic uncertainties from the acceptance corrections are between 5% to 10% depending on the kinematics.

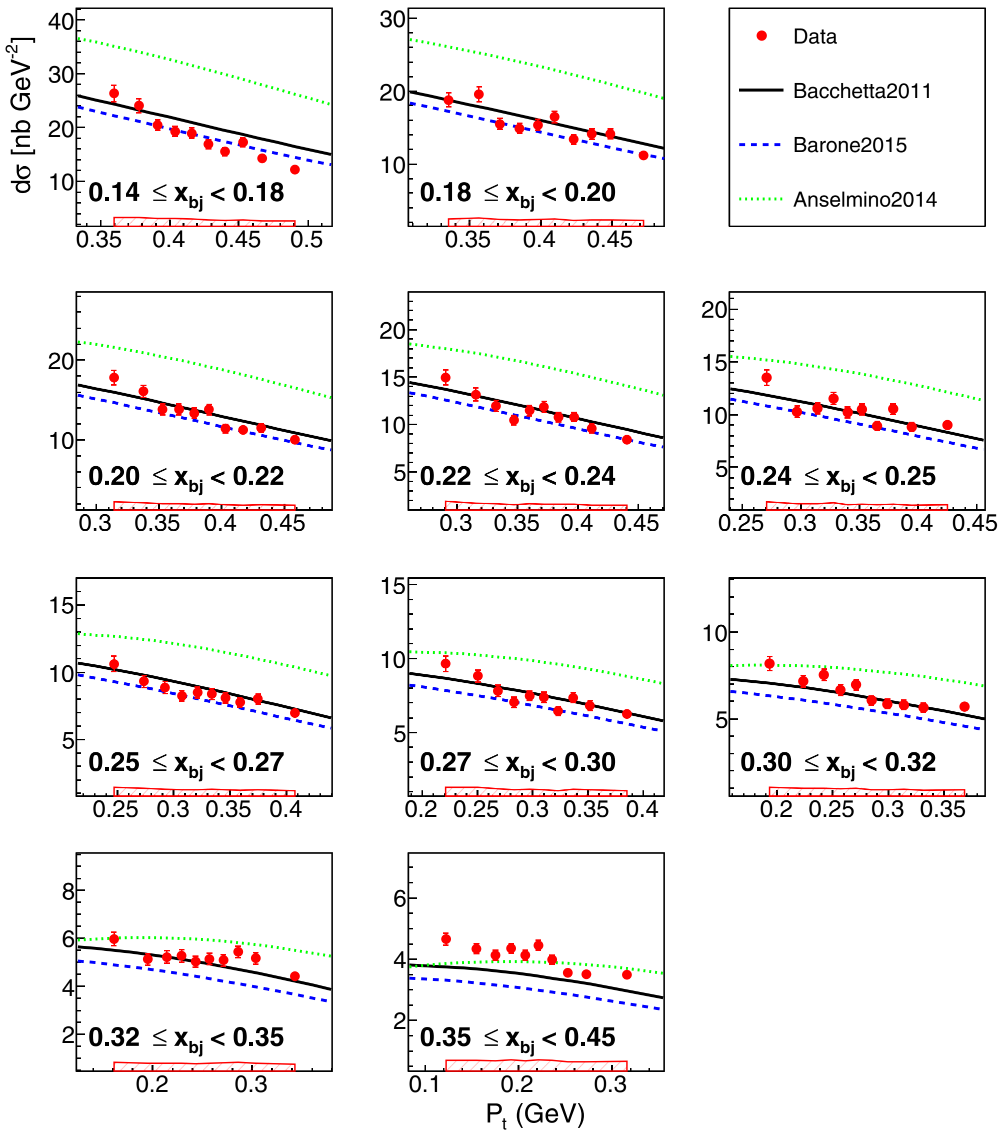

FIG. 8. The differential cross sections in 2D bins: the π^+ SIDIS production channel. The red circles are from the data, the black solid lines are from the model [17], the blue dashed lines are from the model [15] and the green dotted lines are from the model [16]. The error bars represent the statistical uncertainties of the data. The error band on the bottom of each panel represents the experimental systematic uncertainty. The x_{bj} range of each plot is presented at the bottom of the panel.

The systematic uncertainties related to the exclusive tail subtractions and the SIDIS radiative corrections have been evaluated in the same manner as in Ref. [22]. Specifically, different models of the exclusive channels and the difference between the HAPRAD and the SIMC for the radiative corrections have been used to define the systematic uncertainties. The systematic uncertainties for these items are between 2% to 6% depending on the kinematics.

The systematic uncertainties of the results related to the central-value uncertainties of the variables (x_{bj}, z_h, Q^2, ϕ_h, P_t) have been evaluated by inserting the variable uncertainties into the bin-centering corrections, thus reflected in the extracted cross sections. The systematic uncertainties related to the bin-centering corrections are less than 3% with a kinematic dependence.

The main contributions of the systematic uncertainties are listed in Table I.

E. Kinematical correlations and binning

In the production run of E06-010, only one experimental configuration was used. Kinematical correlations are shown in Fig. 5. Due to the kinematical correlations, strict one-dimensional (1D) binning in which only one variable changes while all the other variables stay intact is prohibited.

In this paper, a set of pseudo-one-dimensional (pseudo-1D) bins is used for presenting the results. Pseudo-1D means that, when the binning is in one variable, for example, x_{bj}, the difference between one bin and another is not only in x_{bj}, but in all the variables (x_{bj}, z_h, Q^2, ϕ_h, P_t) due to kinematical correlations. Pseudo-1D bins in x_{bj} has 10 consecutive bins

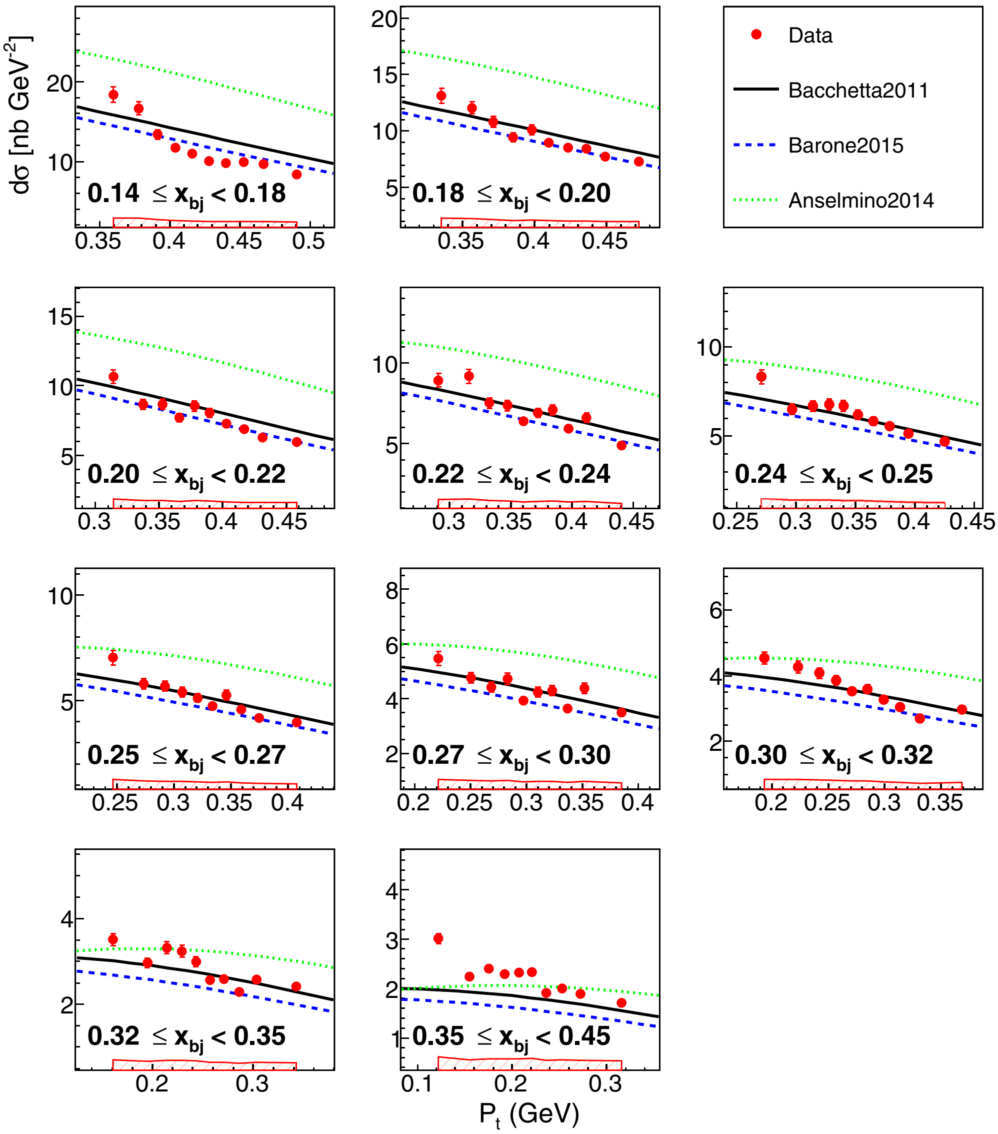

FIG. 9. The differential cross sections in 2D bins: the π^- SIDIS production channel. The definitions of the markers, the lines, and the bands are the same as in Fig. 8 for the π^+ channel.

with almost equal statistics. The central values of the kinematic variables in the pseudo-1D bins are presented in Table II.

As shown in Fig. 5 and Table II the acceptance in this experiment had strong kinematic correlations. In increasing range of x_{bj}, z_h, and Q^2 also increased, while P_t decreased. The kinematic range of ϕ_h centered around the angle of π (180°), due to the experimental configuration. The central values of ϕ_h and x_{bj} were weakly correlated. In the range of ϕ_h closer to the center more events were with smaller x_{bj} compared with the range of ϕ_h farther from the center.

A set of two-dimensional (2D) bins is used to present the P_t dependence of the cross sections. The set of 2D bins (10×10) consists of $10 P_t$ bins in 10 ranges of x_{bj}. The boundaries of the bins are set to make each bin contain almost equal statistics.

A set of three-dimensional (3D) bins is used to present the ϕ_h dependence of the cross sections. The data are binned into two ranges of P_t first. In each of the P_t ranges, five x_{bj} bins are defined. In each of the 2×5 ranges of P_t vs x_{bj}, $10 \phi_h$ bins are defined. Each bin of the $2 \times 5 \times 10$ set has almost equal statistics.

V. RESULTS

The extracted unpolarized SIDIS differential cross sections and the cross-section ratios are compared with models in different bin sets in the following sections. Fitting the extracted differential cross sections from these data demonstrates the data's constraint on the parameters describing the SIDIS process. The plane-wave impulse approximation (PWIA) treatment of the ^{3}He nucleus in the SIDIS process is adopted in this study, thus the modeled SIDIS cross section from ^{3}He is the same as the sum of the modeled SIDIS differential cross sections from two protons and one neutron. The collinear PDF from CTEQ10 [58] and the collinear FF from DSS [59] were used in the modeled SIDIS differential cross sections.

In the multidimensional bin sets, models from three studies [15–17] are compared with the data. The modeled SIDIS differential cross sections were calculated as in Eq. (1) by using the parameters $\langle k_\perp^2 \rangle$ and $\langle p_\perp^2 \rangle$ from these three studies. The parametrizations of the Boer–Mulders TMD PDF and the Collins TMD FF were taken from Ref. [15], giving a negligible (less than 2%) contribution to the SIDIS differential cross sections.

In Ref. [15], the multiplicity data and azimuthal-modulation data from HERMES [24,26] were simultaneously fit. The multiplicity data from COMPASS [25] were further normalized before combining with the azimuthal-modulation data from COMPASS [27] for the simultaneous fit. The Gaussian width $\langle k_\perp^2 \rangle$ was set as a free fitting parameter while the Gaussian width $\langle p_\perp^2 \rangle$ was parametrized as $\langle p_\perp^2 \rangle = A + Bz_h^2$. The A and B were the other two free fitting parameters. The minimal χ^2 fitting results using the HERMES data were $\langle k_\perp^2 \rangle = 0.037 \pm 0.004$ GeV^2, $A = 0.126 \pm 0.004$ GeV^2, and $B = 0.506 \pm 0.045$ GeV^2. The minimal χ^2 fitting results using the COMPASS data were $\langle k_\perp^2 \rangle = 0.031 \pm 0.006$ GeV^2, $A = 0.200 \pm 0.002$ GeV^2, and $B = 0.571 \pm 0.018$ GeV^2. The Boer–Mulders TMD PDF and Collins TMD FF were also parametrized and included in the fitting in the study [15]. The SIDIS differential cross sections using the parameters $\langle k_\perp^2 \rangle = 0.037$ GeV^2 and $\langle p_\perp^2 \rangle = 0.126 + 0.506 z_h^2$ GeV^2 are denoted as “Barone2015” representing the model from Ref. [15] in the comparisons between the data and the models (Figs. 6–9).

In Ref. [16], the multiplicity data from HERMES [24] and COMPASS [25] were fit while the azimuthal-modulation data were not included in the fitting process. The results of fitting the HERMES data were $\langle k_\perp^2 \rangle = 0.57 \pm 0.08$ GeV^2 and $\langle p_\perp^2 \rangle = 0.12 \pm 0.01$ GeV^2. The fitting quality was satisfactory ($\chi^2_{\text{dof}} = 1.69$), and the $\langle k_\perp^2 \rangle$ value is an order of magnitude larger than the value in Ref. [15]. The results of fitting the COMPASS data were $\langle k_\perp^2 \rangle = 0.61 \pm 0.20$ GeV^2 and $\langle p_\perp^2 \rangle = 0.19 \pm 0.02$ GeV^2. Comparing with the HERMES-data fitting, the COMPASS-data fitting quality was much worse ($\chi^2_{\text{dof}} = 8.54$), while a similar $\langle k_\perp^2 \rangle$ value was found. The SIDIS differential cross sections using the parameters $\langle k_\perp^2 \rangle = 0.57$ GeV^2 and $\langle p_\perp^2 \rangle = 0.12$ GeV^2 are denoted as “Anselmino2014” representing the model from Ref. [16] in the comparisons between the data and the models (Figs. 6–9).

In Ref. [17], $\langle k_\perp^2 \rangle = 0.14$ GeV^2 and $\langle p_\perp^2 \rangle = (0.42) z_h^{0.54} (1 - z_h)^{0.37}$ GeV^2 from a HERMES study [60] were fixed when carrying out simultaneous fitting of the nucleon magnetic moments and the semi-inclusive SSAs. We denote this set of parameters as “Bacchetta2011” representing the model from Ref. [17] in the comparisons between the data and the models (Figs. 6–9, 11, and 12).

In all the bin sets, some of the kinematic variables were not separated in multiple ranges and were treated as in a single bin (single-binned variables). The central values and ranges of the single-binned variables changed in different bins due to the kinematic correlations. The central values of the variables were determined by using Eq. (19). We kept the single-binned-variables in the definition of the differential cross sections and kept the differential phase space in the results as $d\text{PHS} = dx_{bj} dy dz_h d\phi_S dP_t^2 d\phi_h$ in all the bin sets. The method to extract the differential cross section for a specific bin was discussed in Sec. IV C.

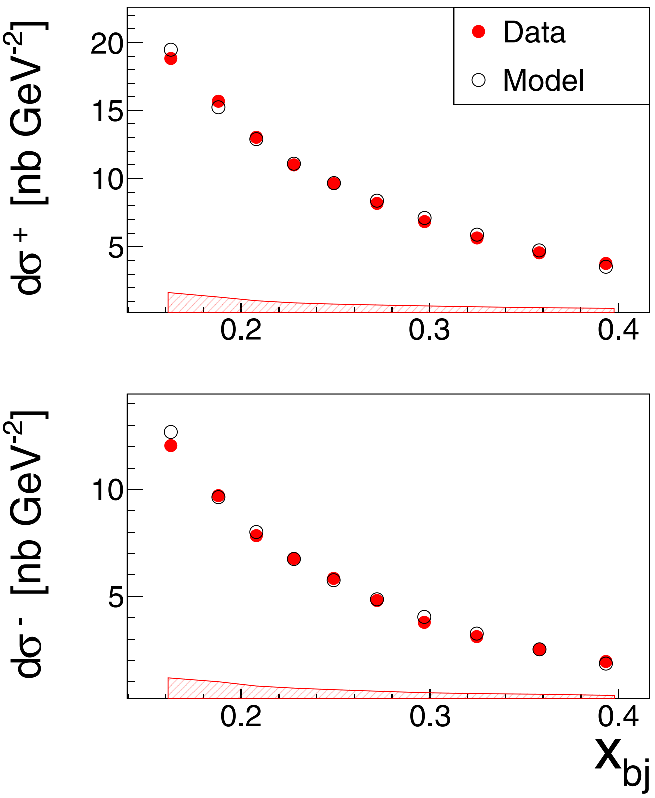

FIG. 10. The SIDIS differential cross sections (defined in text) comparison between the data and the simulation in pseudo-1D x_{bj} bins. The red solid circles are from the data and the black open circles are from the quark-parton model. The error bar of each point represents the statistical uncertainty, mostly smaller than the markers. The error band on the bottom of each panel represents the experimental systematic uncertainty. The top and bottom panels are for π^+ and π^- production channels, respectively.

In all the bin sets the data corrections in Eqs. (11) and (18) were carried out in the same way for individual bins. The BCCs defined in Eq. (20) were carried out differently in pseudo-1D bins and multidimensional bins.

In pseudo-1D bins, the central values of all the kinematic variables were the experimental averages using Eq. (19). The BCCs were evaluated by using these central values of the kinematics. The differential cross sections from the model were at the same central values of the kinematics.

In the multidimensional bin sets, the dependence of the differential cross section on one kinematic variable (ϕ_h or P_t) was examined in multiple ranges of other variables. To remove the effect of kinematical correlations, BCCs were evaluated with range-by-range sets of kinematics. In each range, the corresponding set of kinematic variables was put in the model $\sigma_{\text{theory}} = \sigma_{\text{model}}(\text{vars})$ of Eq. (20) while the ratio $\sigma^{\text{bin}}_{\text{expt}} / \sigma^{\text{bin}}_{\text{MC}}$ in Eq. (20) was evaluated in the usual way for each bin. In each of the range-by-range sets of kinematics, the variable of interest (ϕ_h or P_t) had the experimental-averaged value for each bin, while all the other variables had the experimental-averaged value at the central bin in this range.

We did not combine different ranges of the multidimensional bin sets to give one distribution of the variable of interest, for minimizing the model dependence introduced in the BCCs.

A. Cross sections in pseudo-1D bins

The comparisons of the SIDIS differential cross sections from the data and the quark-parton model in pseudo-1D x_{bj} bins are shown in Fig. 10. The top panel in the figure is for the π^+ production channel ^{3}He(e,e$'\pi^+$)X and the bottom panel for the π^- production channel ^{3}He(e,e$'\pi^-$)X. The vertical axis is the SIDIS differential cross section $d\sigma/(dx_{bj}dydz_hd\phi_S dP_t^2 d\phi_h)$ in unit of nb GeV^{-2} rad^{-2}. The total experimental systematic uncertainties using quadrature combination of all the sources are shown in the band at the bottom of each plot.

The SIDIS differential cross section from the model is defined in Eq. (1) and the parametrizations of the Gaussian widths of unpolarized TMD PDF and FF are in the forms as in Ref. [17]; namely, $\langle k_\perp^2\rangle = 0.14$ GeV^2 and $\langle p_\perp^2\rangle = az_h^{0.54}(1-z_h)^b$ GeV^2, where $a = 1.55$ and $b = 2.2$ are tuned from the values in one set of the HERMES data analysis inherited and cited by Ref. [17]. The Boer–Mulders TMD PDF and Collins TMD FF parametrizations were taken from Ref. [15]. The effect of the Boer–Mulders terms in the total SIDIS cross sections were found to be less than 2% in magnitude and opposite in sign for the $\pi^\pm$ electroproduction channels. Terms with twists higher than those included in Sec. II were neglected.

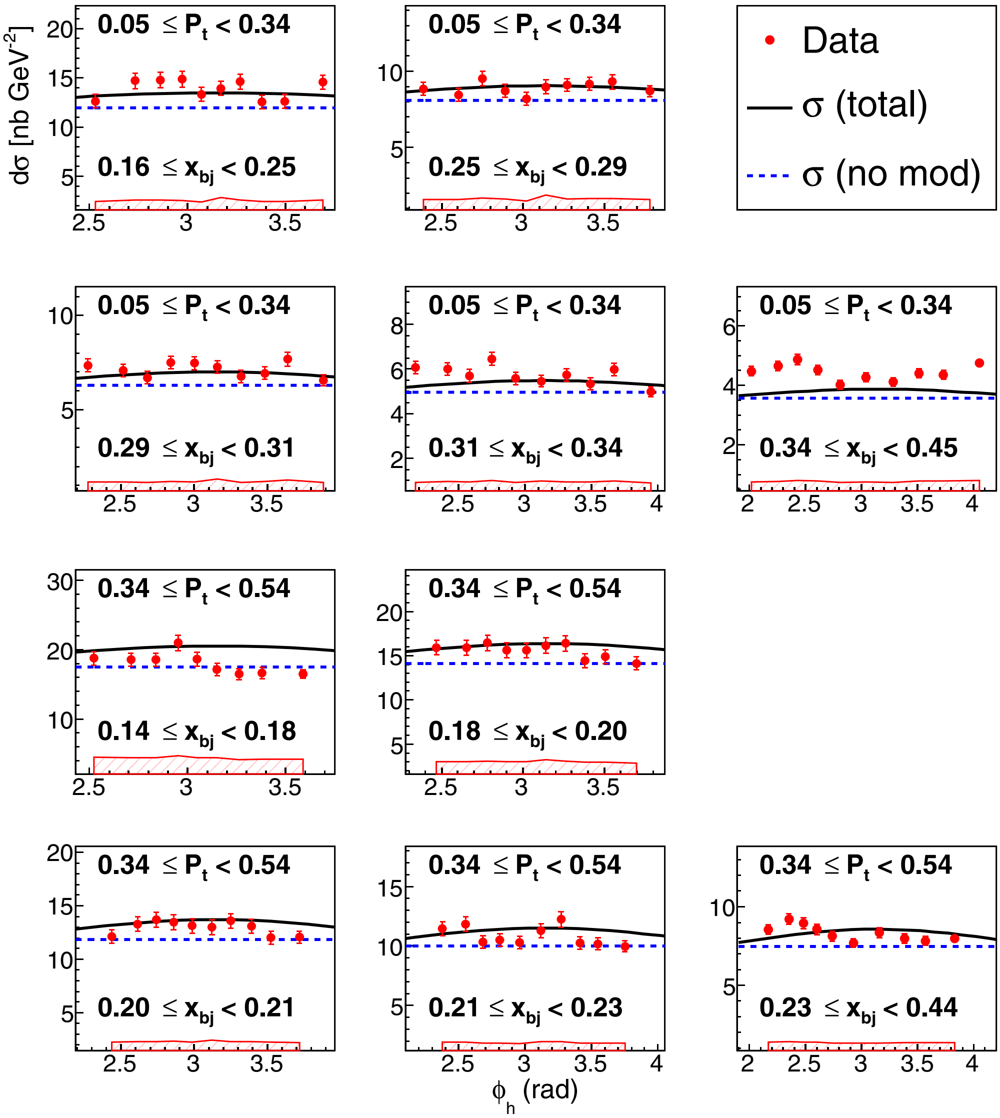

FIG. 11. The differential cross sections in 3D bins: the π^+ SIDIS production channel. The red circles are from the data, the black solid lines are from the model [17], and the blue dashed lines are from the model [17] with $F_{UU}^{\cos\phi_h}$ and $F_{UU}^{\cos 2\phi_h}$ set to zero. The error bars represent the statistical uncertainties of the data. The error band on the bottom of each panel represents the experimental systematic uncertainty. The P_t (in unit of GeV) and x_{bj} ranges of each plot are presented at the top and the bottom of the panel, respectively.

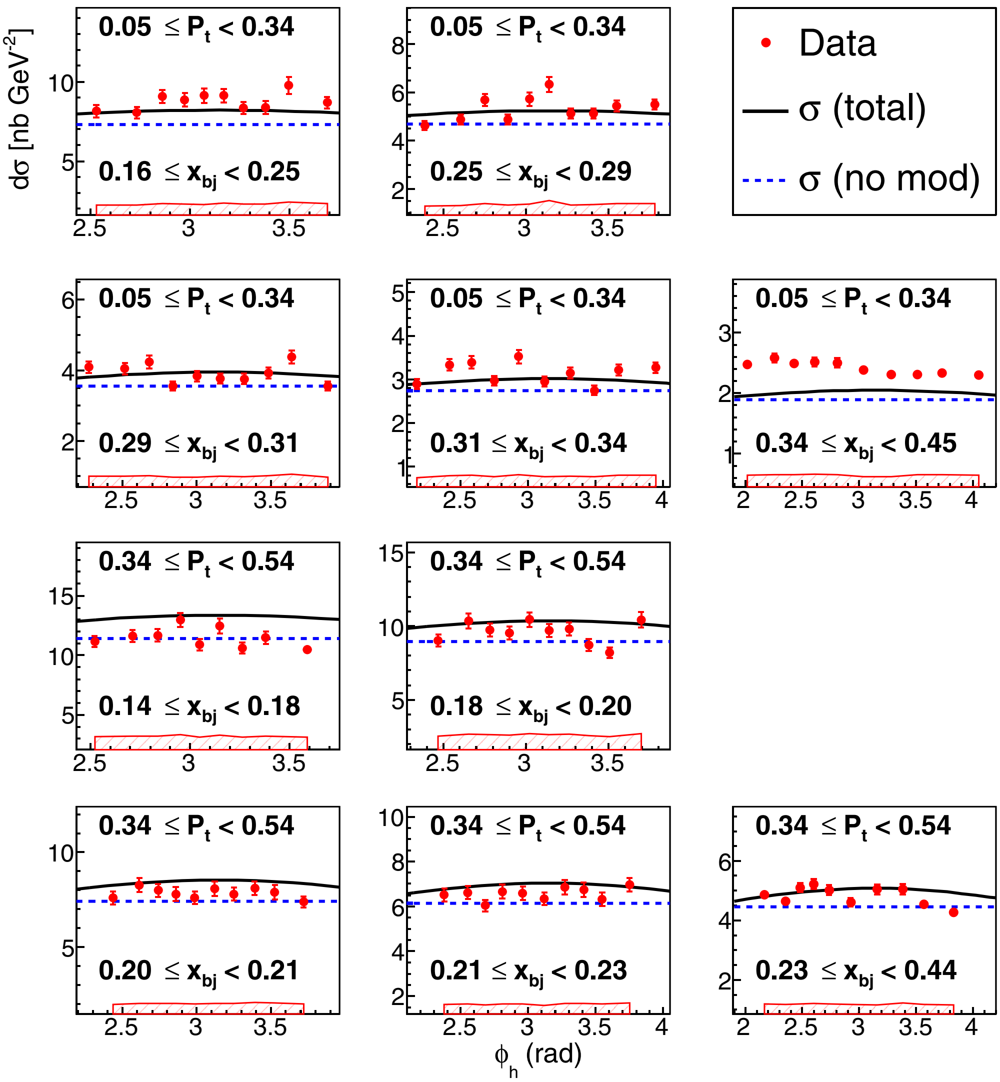

FIG. 12. The differential cross sections in 3D bins: the π^- SIDIS production channel. The definitions of the markers, the lines, and the bands are the same as the figure above for the π^+ channel.

The model calculates the sum of the cross sections from two protons and one neutron as an approximation for the ^{3}He nucleus.

Agreement between the data and the model is observed. The cross sections and corresponding kinematic variables are presented in Tables III and IV in Appendix.

B. ϕ_h dependence of cross sections

The differential cross sections of SIDIS were extracted in 3D bins ($2 \times 5 \times 10$) to examine the ϕ_h dependence of the cross sections in 2×5 ranges of P_t vs x_{bj}. Bin-centering corrections were used to remove the difference of all the variables except ϕ_h from one bin to another in each of the P_t vs x_{bj} ranges, therefore the $10\phi_h$ bins in a certain range of P_t and x_{bj} differ only in the values of ϕ_h. The comparisons of the SIDIS differential cross sections from the data and the models from Refs. [15–17] are presented in Figs. 6 and 7.

Comparisons between the data and the model from Ref. [17] with and without modulations are in Figs. 11 and 12. In the model, the modulations are from the structure functions $F_{UU}^{\cos\phi_h}$ and $F_{UU}^{\cos 2\phi_h}$ on the top of the nonmodulated part (F_{UU}). The distributions from the model without modulations were calculated by using the model parametrization while setting $F_{UU}^{\cos\phi_h}$ and $F_{UU}^{\cos 2\phi_h}$ to zero.

The comparisons show that the model from Ref. [17] compares the best with the data, while the model from Ref. [16] deviates the most from the data in most of the kinematic ranges.

The cross sections and corresponding kinematic variables are presented in Tables V and VI in Appendix.

C. P_t dependence of cross sections

To present the P_t dependence of the SIDIS cross sections, 2D bins (10×10) of x_{bj} vs P_t are used. Bin-centering corrections were used to remove the difference of all the variables except P_t from one bin to another in each range of

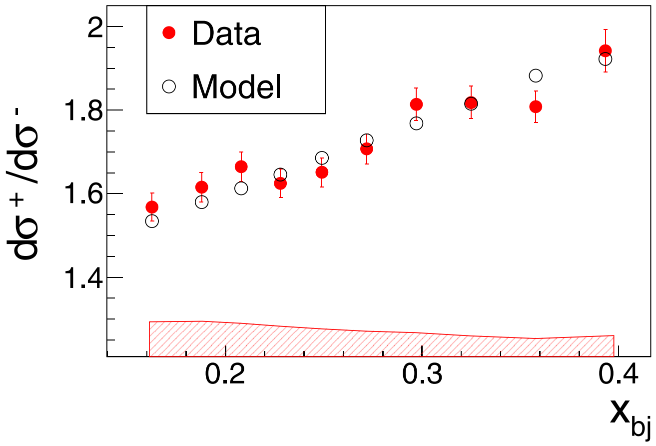

FIG. 13. The SIDIS differential cross section ratio $\sigma^{\pi^+}/\sigma^{\pi^-}$ comparison between data and model in pseudo-1D x_{bj} bins. The red solid circles are from the data and the black open circles are from the quark-parton model. The error bar of each point of data represents the statistical uncertainty. The error bars for the model parametrization uncertainty are smaller than the marker size. The error band on the bottom represents the systematic uncertainty of the data.

x_{bj}, therefore the 10P_t bins in a certain range of x_{bj} differ only in the values of P_t. The comparisons of the SIDIS differential cross sections from the data and the models from Refs. [15–17] are presented in Figs. 8 and 9.

The comparisons show that the model from Ref. [17] compares the best with the data, while the model from Ref. [16] deviates the most from the data in most of the kinematic ranges. In the highest x_{bj} ranges (corresponding to the lowest P_t ranges), the model from Ref. [16] gives better comparison than the models from Refs. [15,17], but still has sizable deviations from the data.

The cross sections and corresponding kinematic variables are presented in Tables VII and VIII in Appendix.

D. Ratios of cross sections

The comparisons of the ratios (from the data and the model) of SIDIS π^+ production cross sections over SIDIS π^- production cross sections in pseudo-1D x_{bj} bins are shown in Fig. 13. The model parameters are the same as in Sec. V A. The systematic uncertainties from the acceptance and efficiency of electron detection in BigBite are not included in the bottom systematic error band, because the electron part is the same in the SIDIS $\pi^\pm$ production.

In the plot, the error bars of the data points are for the statistical uncertainties of the data. The error bars of the model points are for the model uncertainties. In this study, the model uncertainties are defined by the quadrature combination of the differences of the ratios with and without the contribution from the Boer–Mulders terms, changing the width $\langle k_\perp^2\rangle$ to $2\langle k_\perp^2\rangle$ and changing $\langle p_\perp^2\rangle$ to $2\langle p_\perp^2\rangle$. The Boer–Mulders effects in the $\pi^\pm$ production channels have opposite signs, and the changes of the cross-section ratios due to turning off the Boer–Mulders contributions are 1% to 4%. The flavor dependence of the widths has not been included in the model, thus the widths do not differ in channels of the $\pi^\pm$ production. Theoretically, if the $\pi^\pm$ SIDIS production cross sections have the same transverse-momentum dependence, their ratios at the same kinematics will be independent of the widths. Due to the very small differences between the central values of variables in the $\pi^\pm$ production channels, the effect of changing $\langle k_\perp^2\rangle$ to $2\langle k_\perp^2\rangle$ or $\langle p_\perp^2\rangle$ to $2\langle p_\perp^2\rangle$ was nonzero but less than 0.1%.

Results from the data are consistent with the model without a flavor dependence of $\langle k_\perp^2\rangle$ and $\langle p_\perp^2\rangle$ as assumed in most of the global analysis for SIDIS [15–17].

E. Azimuthal modulation and stand-alone data fitting

Fitting the ϕ_h distribution in each of the 2 × 5 ranges of P_t vs x_{bj} in the 3D bins (2 × 5 × 10), with a simple function $A(1 - B\cos\phi_h)$, provides a naive probe for the azimuthal modulation effect in the data. The parameter B indicates the size of the modulation. The parameter Bs in all ranges are presented in Fig. 14. Due to a limited ϕ_h range in the data and a large number of fitting parameters being used (A and B in one P_t and x_{bj} range differ from A and B in another range), the data do not provide good constraints on the values for B.

Azimuthal modulation effects in the unpolarized SIDIS channel arise from the relative magnitudes of $F_{UU}^{\cos\phi_h}$, $F_{UU}^{\cos 2\phi_h}$, and F_{UU}. By using the functional forms in Sec. II, F_{UU} and the Cahn parts of the structure functions $F_{UU}^{\cos\phi_h}$ and $F_{UU}^{\cos 2\phi_h}$ after convolution can be expressed as

$$F_{UU} = \sum_q f_q^c D_q^c \frac{e_q^2 x_{bj}}{\pi\langle P_t^2\rangle} e^{-P_t^2/\langle P_t^2\rangle}, \tag{22}$$

$$F_{UU}^{\cos\phi_h} = -2\sum_q f_q^c D_q^c \frac{P_t z_h e_q^2 x_{bj}\langle k_\perp^2\rangle}{\pi Q\langle P_t^2\rangle^2} e^{-P_t^2/\langle P_t^2\rangle}, \tag{23}$$

$$F_{UU}^{\cos 2\phi_h} = 2\sum_q f_q^c D_q^c \frac{P_t^2 z_h^2 e_q^2 x_{bj}\langle k_\perp^2\rangle^2}{\pi Q^2\langle P_t^2\rangle^3} e^{-P_t^2/\langle P_t^2\rangle}, \tag{24}$$

where $\langle P_t^2\rangle = \langle p_\perp^2\rangle + z_h^2\langle k_\perp^2\rangle$. The Boer–Mulders parts after convolution can be found in Ref. [15].

The parameters being fit are the Gaussian widths $\langle k_\perp^2\rangle$ and $\langle p_\perp^2\rangle$, while the Boer–Mulders parts set to zero. The 2D bins (10 × 10) and 3D bins (2 × 5 × 10) data were fit and the results are in Fig. 15. Three contours corresponding to $\delta\chi^2 = 1$, 2.3, and 6.2 are drawn besides the central values from the fitting. The $\delta\chi^2 = 1$ contour is conventionally the same as the one-σ contour. The contours of $\delta\chi^2 = 2.3$ and 6.2 show the constraints of two-parameter fitting at confidence levels of 68% and 95%, respectively. The central values of the fitting in the 2D bins are $\langle k_\perp^2\rangle = 0.003 \pm 0.008$ GeV^2 and $\langle p_\perp^2\rangle = 0.2104 \pm 0.0025$ GeV^2. The central values of the fitting in the 3D bins are $\langle k_\perp^2\rangle = 0.006 \pm 0.010$ GeV^2 and $\langle p_\perp^2\rangle = 0.2148 \pm 0.0026$ GeV^2. The fitting results indicate consistent azimuthal modulation effects from the data in 3D bins with the ϕ_h information and 2D bins without the ϕ_h information.

Fitting the data with a simpler functional form; namely, setting $F_{UU}^{\cos\phi_h}$ and $F_{UU}^{\cos 2\phi_h}$ to zero, was also done. The results are presented in Fig. 16. The central values of the fitting in the 2D bins are $\langle k_\perp^2\rangle = 0.090 \pm 0.097$ GeV^2 and

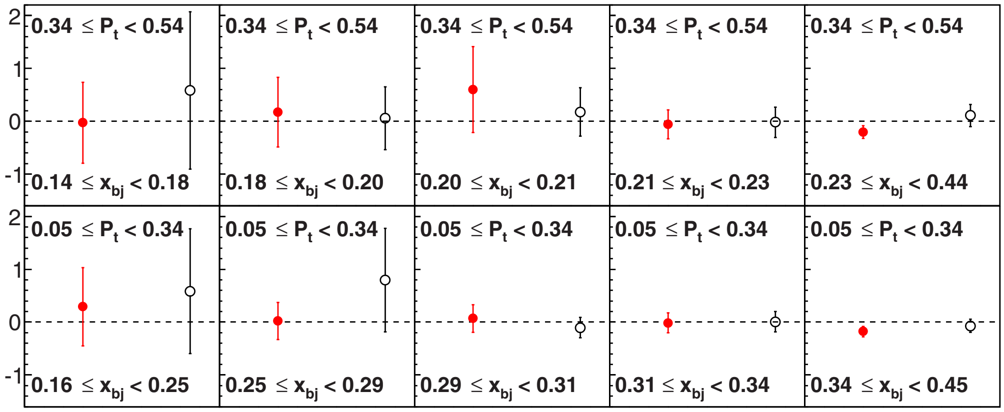

FIG. 14. Results of B in 3D bins from the $A(1 - B\cos\phi_h)$ fit. The red solid circles and black open circles represent the results in the π^+ and π^- production channels, respectively.

$\langle p_\perp^2\rangle = 0.1840 \pm 0.0276$ GeV^2. The central values of the fitting in the 3D bins are $\langle k_\perp^2\rangle = 0.085 \pm 0.112$ GeV^2 and $\langle p_\perp^2\rangle = 0.1901 \pm 0.0330$ GeV^2.

The very different constraints of $\langle k_\perp^2\rangle$ vs $\langle p_\perp^2\rangle$ using the functional form including all three structure functions (Fig. 15) and the functional form including only the structure function F_{UU} (Fig. 16), come from the specific model formulation; namely, $F_{UU}^{\cos\phi_h}$ and $F_{UU}^{\cos 2\phi_h}$ as in Eqs. (23) and (24). These specific functional forms, when applied to the data in this study, would result in the intrinsic transverse momentum width $\langle k_\perp^2\rangle$ of the quarks in the nucleon being consistent with zero at small central values, which contradicts the results from the global analyses [15–17]. The effect of including the Boer–Mulders terms as parametrized in Ref. [15] was tested to be negligible (less than 2% in the kinematic range of this study).

To examine the data's constraint on the intrinsic widths with relaxed model formulations, two adjusted functional forms were used to do the fitting in the 3D bins with the ϕ_h information. The first one includes the structure functions F_{UU} and $F_{UU}^{\cos\phi_h}$, with an additional fitting parameter A to tune the amplitude of modulation as $AF_{UU}^{\cos\phi_h}$. The results of the fitting are $\langle k_\perp^2\rangle = 0.078 \pm 0.1505$ GeV^2, $\langle p_\perp^2\rangle = 0.1925 \pm 0.0464$ GeV^2, and $A = 0.0119 \pm 0.1971$. The intrinsic widths $\langle k_\perp^2\rangle$ and $\langle p_\perp^2\rangle$ are under loose constraint individually while the amplitude of $AF_{UU}^{\cos\phi_h}$ is suppressed by a small factor A.

The second one includes the structure functions F_{UU}, $F_{UU}^{\cos\phi_h}$, and $F_{UU}^{\cos 2\phi_h}$, with an additional fitting parameter A to tune the amplitude of modulation as $A(F_{UU}^{\cos\phi_h} + F_{UU}^{\cos 2\phi_h})$.

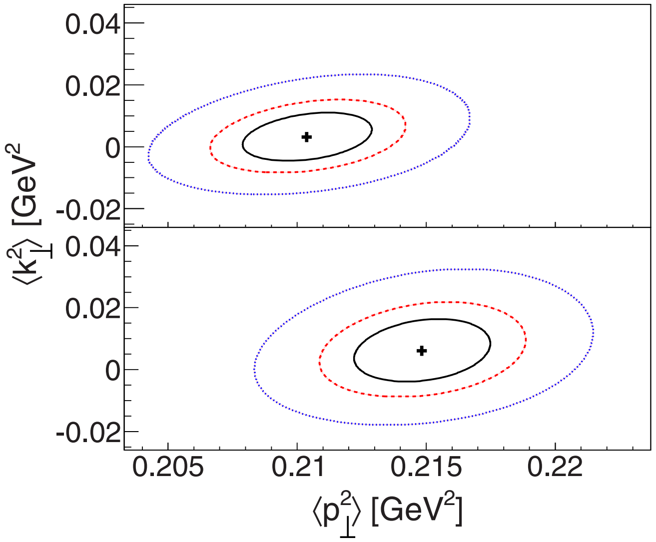

FIG. 15. Fitting contours with the functional form of the total unpolarized SIDIS cross section (refer to the text). The top panel is for the fitting results using the 2D bins (10 × 10) data, the bottom panel for the 3D bins (2 × 5 × 10). The central values of the fitting are the black crosses. The three contours from the smallest to the largest in each panel correspond to $\delta\chi^2 = 1$, 2.3, and 6.2, respectively.

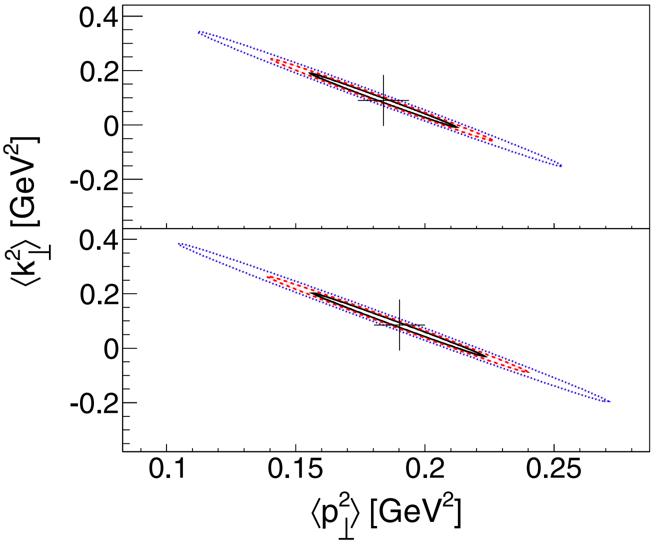

FIG. 16. Fitting contours with the functional form of the nonmodulated unpolarized SIDIS cross section ($F_{UU}^{\cos\phi_h}$ and $F_{UU}^{\cos 2\phi_h}$ set to zero; refer to the text). The top panel is for the fitting results using the 2D bins (10 × 10) data, the bottom panel for the 3D bins (2 × 5 × 10). The central values of the fitting are the black crosses. The three contours from the smallest to the largest in each panel correspond to $\delta\chi^2 = 1$, 2.3, and 6.2, respectively.

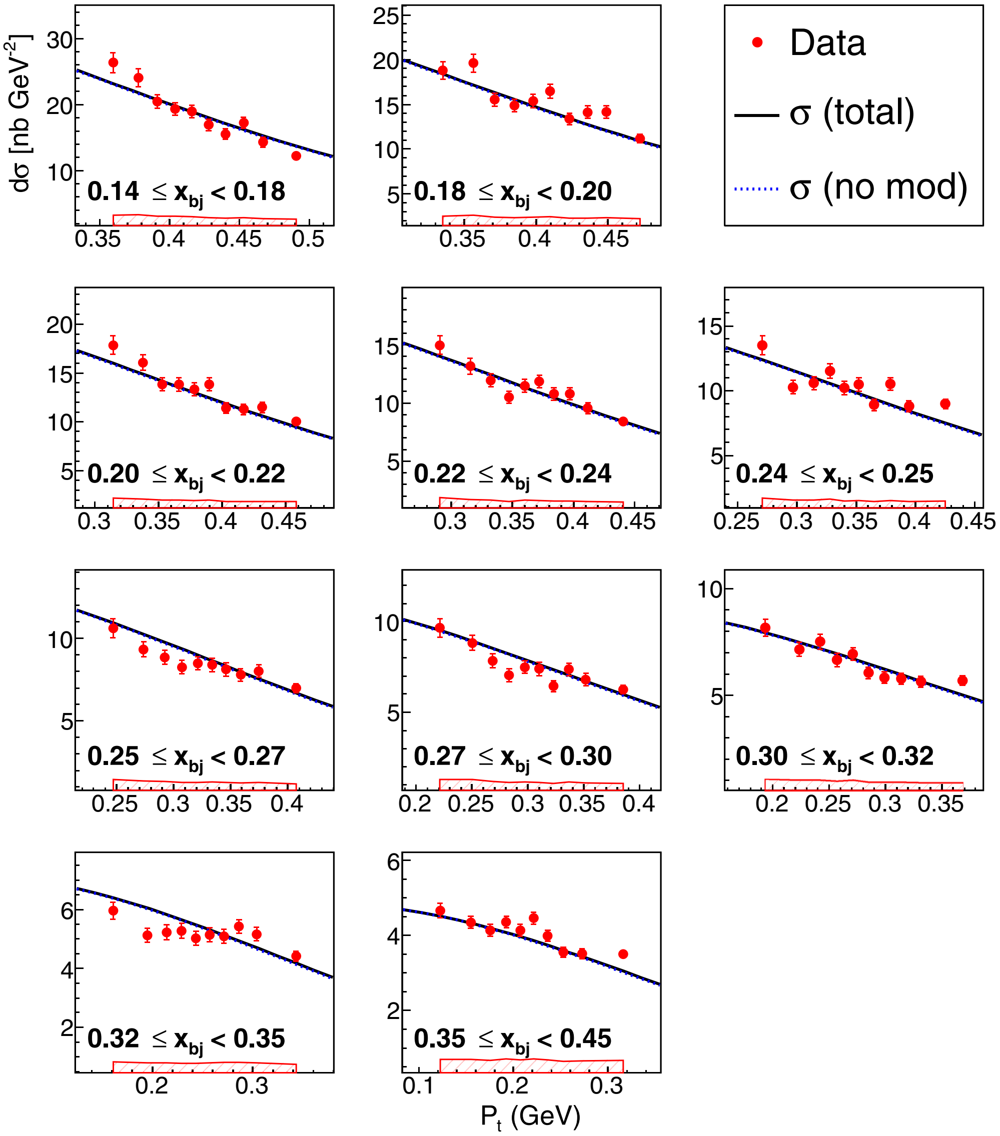

FIG. 17. The differential cross sections in 2D bins: the π^+ SIDIS production channel. The red circles are from the data. The black solid lines are from the model including the structure functions F_{UU}, $F_{UU}^{\cos\phi_h}$, and $F_{UU}^{\cos 2\phi_h}$ with parameters $\langle k_\perp^2\rangle$ and $\langle p_\perp^2\rangle$ from stand-alone data fitting. The blue dashed lines are from the model including only the structure functions F_{UU} with parameters $\langle k_\perp^2\rangle$ and $\langle p_\perp^2\rangle$ from fitting the data of this work only. The error bars represent the statistical uncertainties of the data. The error band on the bottom of each panel represents the experimental systematic uncertainty. The x_{bj} range of each plot is presented at the bottom of the panel.

The results of the fitting are $\langle k_\perp^2\rangle = 0.080 \pm 0.1542$ GeV^2, $\langle p_\perp^2\rangle = 0.1918 \pm 0.0475$ GeV^2, and $A = 0.0077 \pm 0.1820$. The intrinsic widths are under similar constraint as in the first case with a small factor A suppressing the amplitude of $A(F_{UU}^{\cos\phi_h} + F_{UU}^{\cos 2\phi_h})$.

Without introducing specific forms of $F_{UU}^{\cos\phi_h}$ and $F_{UU}^{\cos 2\phi_h}$, the parameters $\langle k_\perp^2\rangle$ and $\langle p_\perp^2\rangle$ in the SIDIS channels appear as the combined quantity $\langle P_t^2\rangle$. Sensitivity to $\langle P_t^2\rangle$ is explicitly provided by the P_t behavior of the data. The comparison between the data and the models in the two functional forms (with and without $F_{UU}^{\cos\phi_h}$ and $F_{UU}^{\cos 2\phi_h}$) using the parameters from fitting in 2D bins of the data are shown in Figs. 17 and 18.

VI. CONCLUSION

We report the first measurement of the unpolarized SIDIS differential cross section of $\pi^\pm$ production from a ^{3}He target in a kinematic range $0.12 < x_{bj} < 0.45$, $1 < Q^2 < 4$ (GeV/c)^2, $0.45 < z_h < 0.65$, and $0.05 < P_t < 0.55$ GeV/c.

In the multidimensional bin sets, the data are compared with three models from Refs. [15–17] while the ^{3}He nucleus approximated as two protons and one neutron in a plane-wave picture. In most of the kinematic ranges, the model from Ref. [17] compares the best with the data while the model from Ref. [16] deviates the most from the data. In the highest x_{bj} ranges (corresponding to the lowest P_t ranges), the model from Ref. [16] gives the best comparison with the data.

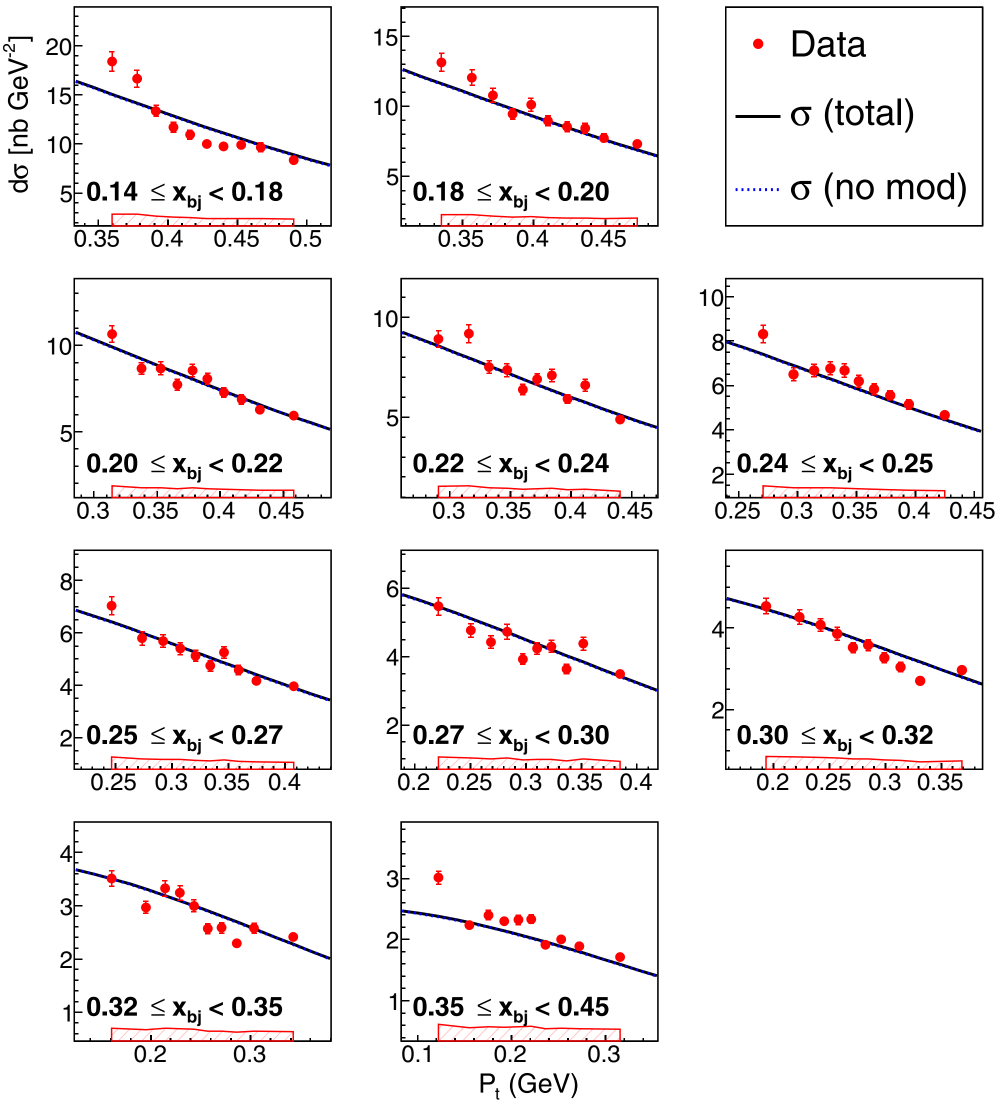

FIG. 18. The differential cross sections in 2D bins: the π^- SIDIS production channel. The definitions of the markers, the lines, and the bands are the same as the figure above for π^+ channel.

TABLE III. Unpolarized SIDIS cross section, uncertainties, and central value of variables in π^+ channel: pseudo-1D x_{bj} bins. The variable defining the bins (x_{bj}) is listed in the first column. The following columns are for the unpolarized SIDIS differential cross section, the statistical uncertainty, the systematic uncertainty, and the central values of the kinematic variables in the bins.

x_{bj}	$d\sigma$	Stat.	Sys.	x_{bj}	Q^2	y	z_h	ϕ_h	P_t
0.163	18.77	0.25	1.4	0.163	1.47	0.831	0.476	3.1	0.437
0.188	15.68	0.23	1.1	0.188	1.7	0.818	0.484	3.08	0.411
0.208	13.03	0.18	0.84	0.208	1.85	0.806	0.491	3.07	0.392
0.228	11.01	0.16	0.68	0.228	2	0.793	0.499	3.07	0.371
0.249	9.636	0.13	0.6	0.249	2.14	0.779	0.508	3.06	0.35
0.272	8.181	0.11	0.53	0.272	2.29	0.764	0.519	3.06	0.325
0.297	6.838	0.095	0.46	0.297	2.45	0.747	0.53	3.05	0.299
0.325	5.644	0.078	0.4	0.325	2.62	0.73	0.543	3.05	0.271
0.358	4.547	0.061	0.34	0.358	2.81	0.711	0.557	3.04	0.239
0.393	3.765	0.062	0.28	0.393	3.09	0.703	0.562	3.02	0.216

TABLE IV. Unpolarized SIDIS cross section, uncertainties, and central value of variables in π^- channel: pseudo-1D x_{bj} bins. Each column is define as in the previous table for the π^+ channel.

x_{bj}	$d\sigma$	Stat.	Sys.	x_{bj}	Q^2	y	z_h	ϕ_h	P_t
0.163	12.06	0.17	0.99	0.163	1.47	0.831	0.476	3.1	0.437
0.188	9.704	0.16	0.8	0.188	1.7	0.818	0.484	3.08	0.411
0.208	7.831	0.12	0.6	0.208	1.85	0.806	0.491	3.07	0.393
0.228	6.771	0.11	0.5	0.228	2	0.793	0.499	3.07	0.372
0.249	5.837	0.091	0.43	0.249	2.14	0.779	0.508	3.06	0.35
0.272	4.793	0.075	0.36	0.272	2.29	0.764	0.518	3.06	0.325
0.297	3.769	0.062	0.29	0.297	2.45	0.748	0.53	3.05	0.299
0.325	3.104	0.051	0.25	0.325	2.62	0.73	0.542	3.05	0.271
0.358	2.515	0.04	0.21	0.358	2.81	0.712	0.557	3.03	0.24
0.393	1.939	0.04	0.16	0.393	3.09	0.704	0.561	3.02	0.217

TABLE V. Unpolarized SIDIS cross sections in 3D bins for the π^+ channel. The data are presented in 10 groups, each of which has 10 bins of ϕ_h in one of the 2 × 5 ranges of P_t vs x_{bj}. A group consists of five rows, and each row presents the information of two consecutive ϕ_h bins. Nine columns are used to present the information of each bin: the central values of the kinematic variables, the differential cross section, and the uncertainties. A line is drawn in the middle of the table to separate the information of two bins in one row, for the convenience of reading.

x_{bj}	Q^2	y	z_h	P_t	ϕ_h	$d\sigma$	Stat.	Sys.	x_{bj}	Q^2	y	z_h	P_t	ϕ_h	$d\sigma$	Stat.	Sys.
0.226	1.95	0.783	0.504	0.312	2.53	12.62	0.68	0.83	0.226	1.95	0.783	0.504	0.312	2.73	14.72	0.78	0.98
0.226	1.95	0.783	0.504	0.312	2.86	14.79	0.78	0.96	0.226	1.95	0.783	0.504	0.312	2.97	14.87	0.82	0.92
0.226	1.95	0.783	0.504	0.312	3.07	13.33	0.71	0.79	0.226	1.95	0.783	0.504	0.312	3.17	13.93	0.73	1.2
0.226	1.95	0.783	0.504	0.312	3.27	14.61	0.77	1	0.226	1.95	0.783	0.504	0.312	3.38	12.53	0.67	0.84
0.226	1.95	0.783	0.504	0.312	3.5	12.61	0.71	0.85	0.226	1.95	0.783	0.504	0.312	3.69	14.56	0.7	0.98
0.27	2.26	0.758	0.522	0.287	2.39	8.842	0.43	0.67	0.27	2.26	0.758	0.522	0.287	2.61	8.457	0.42	0.68
0.27	2.26	0.758	0.522	0.287	2.75	9.518	0.47	0.76	0.27	2.26	0.758	0.522	0.287	2.89	8.713	0.43	0.69
0.27	2.26	0.758	0.522	0.287	3.02	8.187	0.42	0.58	0.27	2.26	0.758	0.522	0.287	3.14	8.969	0.47	0.95
0.27	2.26	0.758	0.522	0.287	3.27	9.084	0.43	0.7	0.27	2.26	0.758	0.522	0.287	3.41	9.17	0.44	0.74
0.27	2.26	0.758	0.522	0.287	3.55	9.306	0.47	0.72	0.27	2.26	0.758	0.522	0.287	3.78	8.685	0.37	0.68
0.299	2.45	0.741	0.534	0.267	2.27	7.354	0.35	0.46	0.299	2.45	0.741	0.534	0.267	2.52	7.077	0.34	0.45
0.299	2.45	0.741	0.534	0.267	2.68	6.695	0.32	0.44	0.299	2.45	0.741	0.534	0.267	2.84	7.507	0.35	0.5
0.299	2.45	0.741	0.534	0.267	3	7.471	0.35	0.46	0.299	2.45	0.741	0.534	0.267	3.16	7.268	0.34	0.62
0.299	2.45	0.741	0.534	0.267	3.32	6.759	0.33	0.43	0.299	2.45	0.741	0.534	0.267	3.48	6.93	0.33	0.5
0.299	2.45	0.741	0.534	0.267	3.64	7.676	0.38	0.56	0.299	2.45	0.741	0.534	0.267	3.88	6.556	0.29	0.44
0.327	2.63	0.726	0.546	0.243	2.17	6.066	0.29	0.38	0.327	2.63	0.726	0.546	0.243	2.41	6.014	0.29	0.42
0.327	2.63	0.726	0.546	0.243	2.58	5.696	0.28	0.39	0.327	2.63	0.726	0.546	0.243	2.75	6.46	0.3	0.45
0.327	2.63	0.726	0.546	0.243	2.93	5.579	0.28	0.38	0.327	2.63	0.726	0.546	0.243	3.12	5.458	0.26	0.45
0.327	2.63	0.726	0.546	0.243	3.31	5.735	0.28	0.39	0.327	2.63	0.726	0.546	0.243	3.49	5.343	0.26	0.38
0.327	2.63	0.726	0.546	0.243	3.67	5.981	0.29	0.43	0.327	2.63	0.726	0.546	0.243	3.95	4.986	0.21	0.35
0.371	2.89	0.706	0.561	0.198	2.02	4.479	0.16	0.3	0.371	2.89	0.706	0.561	0.198	2.25	4.664	0.17	0.31
0.371	2.89	0.706	0.561	0.198	2.43	4.881	0.17	0.35	0.371	2.89	0.706	0.561	0.198	2.61	4.518	0.16	0.33
0.371	2.89	0.706	0.561	0.198	2.81	4.022	0.15	0.28	0.371	2.89	0.706	0.561	0.198	3.04	4.278	0.15	0.29
0.371	2.89	0.706	0.561	0.198	3.28	4.116	0.15	0.27	0.371	2.89	0.706	0.561	0.198	3.51	4.402	0.15	0.33
0.371	2.89	0.706	0.561	0.198	3.73	4.355	0.15	0.33	0.371	2.89	0.706	0.561	0.198	4.05	4.764	0.13	0.34
0.163	1.49	0.826	0.48	0.427	2.52	18.78	0.96	2.4	0.163	1.49	0.826	0.48	0.427	2.71	18.58	0.95	2.4
0.163	1.49	0.826	0.48	0.427	2.84	18.59	0.95	2.4	0.163	1.49	0.826	0.48	0.427	2.95	21.01	1.1	2.7
0.163	1.49	0.826	0.48	0.427	3.05	18.68	0.99	2.4	0.163	1.49	0.826	0.48	0.427	3.15	17.14	0.94	2.3
0.163	1.49	0.826	0.48	0.427	3.26	16.49	0.83	2.1	0.163	1.49	0.826	0.48	0.427	3.38	16.66	0.87	2.1
0.163	1.49	0.826	0.48	0.427	3.59	16.49	0.63	2.1	0.163	1.49	0.826	0.48	0.427	3.59	16.49	0.63	2.1
0.187	1.69	0.816	0.486	0.404	2.47	15.93	0.83	1.4	0.187	1.69	0.816	0.486	0.404	2.65	15.89	0.85	1.4
0.187	1.69	0.816	0.486	0.404	2.78	16.45	0.87	1.4	0.187	1.69	0.816	0.486	0.404	2.9	15.63	0.83	1.4
0.187	1.69	0.816	0.486	0.404	3.02	15.61	0.81	1.4	0.187	1.69	0.816	0.486	0.404	3.14	16.14	0.85	1.6
0.187	1.69	0.816	0.486	0.404	3.26	16.38	0.86	1.4	0.187	1.69	0.816	0.486	0.404	3.38	14.45	0.78	1.3
0.187	1.69	0.816	0.486	0.404	3.51	14.89	0.77	1.3	0.187	1.69	0.816	0.486	0.404	3.7	14.13	0.76	1.2
0.205	1.83	0.808	0.49	0.395	2.43	12.14	0.62	0.76	0.205	1.83	0.808	0.49	0.395	2.61	13.3	0.67	0.81
0.205	1.83	0.808	0.49	0.395	2.74	13.7	0.68	0.84	0.205	1.83	0.808	0.49	0.395	2.86	13.47	0.7	0.85
0.205	1.83	0.808	0.49	0.395	2.99	13.12	0.66	0.8	0.205	1.83	0.808	0.49	0.395	3.12	12.99	0.69	0.97
0.205	1.83	0.808	0.49	0.395	3.25	13.6	0.68	0.82	0.205	1.83	0.808	0.49	0.395	3.39	13.09	0.65	0.84
0.205	1.83	0.808	0.49	0.395	3.52	12.01	0.62	0.76	0.205	1.83	0.808	0.49	0.395	3.72	12.06	0.58	0.74
0.223	1.97	0.799	0.496	0.385	2.38	11.45	0.58	0.7	0.223	1.97	0.799	0.496	0.385	2.55	11.84	0.6	0.71
0.223	1.97	0.799	0.496	0.385	2.68	10.32	0.54	0.61	0.223	1.97	0.799	0.496	0.385	2.81	10.5	0.53	0.62
0.223	1.97	0.799	0.496	0.385	2.96	10.29	0.52	0.58	0.223	1.97	0.799	0.496	0.385	3.12	11.29	0.57	0.73
0.223	1.97	0.799	0.496	0.385	3.27	12.24	0.65	0.73	0.223	1.97	0.799	0.496	0.385	3.41	10.24	0.53	0.64
0.223	1.97	0.799	0.496	0.385	3.55	10.18	0.54	0.61	0.223	1.97	0.799	0.496	0.385	3.75	9.974	0.47	0.59
0.256	2.21	0.782	0.507	0.37	2.16	8.558	0.31	0.53	0.256	2.21	0.782	0.507	0.37	2.35	9.222	0.33	0.55
0.256	2.21	0.782	0.507	0.37	2.48	8.955	0.34	0.54	0.256	2.21	0.782	0.507	0.37	2.6	8.573	0.33	0.52
0.256	2.21	0.782	0.507	0.37	2.74	8.131	0.31	0.48	0.256	2.21	0.782	0.507	0.37	2.93	7.682	0.29	0.46
0.256	2.21	0.782	0.507	0.37	3.16	8.364	0.32	0.48	0.256	2.21	0.782	0.507	0.37	3.38	7.965	0.31	0.49
0.256	2.21	0.782	0.507	0.37	3.57	7.827	0.29	0.48	0.256	2.21	0.782	0.507	0.37	3.83	7.988	0.23	0.5

TABLE VI. Unpolarized SIDIS cross sections in 3D bins for the π^- channel. The format is the same as the previous table for the π^+ channel.

x_{bj}	Q^2	y	z_h	P_t	ϕ_h	$d\sigma$	Stat.	Sys.	x_{bj}	Q^2	y	z_h	P_t	ϕ_h	$d\sigma$	Stat.	Sys.
0.225	1.95	0.784	0.504	0.312	2.53	8.15	0.4	0.63	0.225	1.95	0.784	0.504	0.312	2.73	8.051	0.36	0.63
0.225	1.95	0.784	0.504	0.312	2.86	9.074	0.42	0.71	0.225	1.95	0.784	0.504	0.312	2.97	8.864	0.43	0.69
0.225	1.95	0.784	0.504	0.312	3.07	9.121	0.45	0.64	0.225	1.95	0.784	0.504	0.312	3.17	9.126	0.44	0.76
0.225	1.95	0.784	0.504	0.312	3.27	8.339	0.38	0.67	0.225	1.95	0.784	0.504	0.312	3.38	8.385	0.41	0.68
0.225	1.95	0.784	0.504	0.312	3.5	9.762	0.54	0.8	0.225	1.95	0.784	0.504	0.312	3.69	8.691	0.37	0.71
0.27	2.26	0.758	0.522	0.287	2.39	4.631	0.19	0.37	0.27	2.26	0.758	0.522	0.287	2.61	4.884	0.21	0.39
0.27	2.26	0.758	0.522	0.287	2.75	5.697	0.25	0.47	0.27	2.26	0.758	0.522	0.287	2.89	4.874	0.2	0.4
0.27	2.26	0.758	0.522	0.287	3.02	5.723	0.28	0.45	0.27	2.26	0.758	0.522	0.287	3.14	6.335	0.31	0.59
0.27	2.26	0.758	0.522	0.287	3.27	5.131	0.21	0.42	0.27	2.26	0.758	0.522	0.287	3.41	5.135	0.21	0.44
0.27	2.26	0.758	0.522	0.287	3.55	5.442	0.24	0.46	0.27	2.26	0.758	0.522	0.287	3.78	5.5	0.21	0.46
0.299	2.45	0.741	0.534	0.268	2.27	4.09	0.17	0.29	0.299	2.45	0.741	0.534	0.268	2.52	4.044	0.17	0.29
0.299	2.45	0.741	0.534	0.268	2.68	4.24	0.18	0.31	0.299	2.45	0.741	0.534	0.268	2.84	3.557	0.13	0.27
0.299	2.45	0.741	0.534	0.268	3	3.836	0.15	0.27	0.299	2.45	0.741	0.534	0.268	3.16	3.763	0.15	0.29
0.299	2.45	0.741	0.534	0.268	3.32	3.754	0.15	0.28	0.299	2.45	0.741	0.534	0.268	3.48	3.92	0.16	0.31
0.299	2.45	0.741	0.534	0.268	3.64	4.379	0.18	0.35	0.299	2.45	0.741	0.534	0.268	3.88	3.552	0.13	0.27
0.327	2.63	0.727	0.545	0.243	2.18	2.891	0.11	0.21	0.327	2.63	0.727	0.545	0.243	2.41	3.333	0.14	0.25
0.327	2.63	0.727	0.545	0.243	2.58	3.389	0.14	0.26	0.327	2.63	0.727	0.545	0.243	2.75	2.97	0.11	0.23
0.327	2.63	0.727	0.545	0.243	2.93	3.52	0.15	0.27	0.327	2.63	0.727	0.545	0.243	3.12	2.946	0.12	0.23
0.327	2.63	0.727	0.545	0.243	3.31	3.143	0.13	0.24	0.327	2.63	0.727	0.545	0.243	3.49	2.744	0.11	0.22
0.327	2.63	0.727	0.545	0.243	3.67	3.212	0.13	0.26	0.327	2.63	0.727	0.545	0.243	3.95	3.266	0.12	0.26
0.371	2.89	0.706	0.561	0.199	2.02	2.473	0.07	0.18	0.371	2.89	0.706	0.561	0.199	2.26	2.582	0.075	0.2
0.371	2.89	0.706	0.561	0.199	2.43	2.488	0.068	0.19	0.371	2.89	0.706	0.561	0.199	2.61	2.517	0.075	0.2
0.371	2.89	0.706	0.561	0.199	2.81	2.5	0.078	0.2	0.371	2.89	0.706	0.561	0.199	3.04	2.382	0.069	0.16
0.371	2.89	0.706	0.561	0.199	3.28	2.306	0.067	0.16	0.371	2.89	0.706	0.561	0.199	3.51	2.309	0.064	0.19
0.371	2.89	0.706	0.561	0.199	3.73	2.335	0.063	0.2	0.371	2.89	0.706	0.561	0.199	4.05	2.297	0.044	0.18
0.163	1.49	0.826	0.48	0.427	2.52	11.15	0.48	1.1	0.163	1.49	0.826	0.48	0.427	2.71	11.62	0.52	1.1
0.163	1.49	0.826	0.48	0.427	2.84	11.68	0.52	1.1	0.163	1.49	0.826	0.48	0.427	2.95	12.97	0.59	1.3
0.163	1.49	0.826	0.48	0.427	3.05	10.89	0.49	1	0.163	1.49	0.826	0.48	0.427	3.15	12.46	0.65	1.2
0.163	1.49	0.826	0.48	0.427	3.26	10.6	0.46	1	0.163	1.49	0.826	0.48	0.427	3.38	11.47	0.54	1.1
0.163	1.49	0.826	0.48	0.427	3.59	10.47	0.33	1	0.163	1.49	0.826	0.48	0.427	3.59	10.47	0.33	1
0.187	1.69	0.816	0.486	0.404	2.47	9.027	0.39	0.92	0.187	1.69	0.816	0.486	0.404	2.65	10.35	0.5	1.1
0.187	1.69	0.816	0.486	0.404	2.78	9.733	0.44	1	0.187	1.69	0.816	0.486	0.404	2.9	9.54	0.44	0.99
0.187	1.69	0.816	0.486	0.404	3.02	10.44	0.49	1.1	0.187	1.69	0.816	0.486	0.404	3.14	9.7	0.44	1
0.187	1.69	0.816	0.486	0.404	3.26	9.801	0.44	1	0.187	1.69	0.816	0.486	0.404	3.38	8.732	0.41	0.93
0.187	1.69	0.816	0.486	0.404	3.51	8.193	0.35	0.86	0.187	1.69	0.816	0.486	0.404	3.7	10.43	0.53	1.1
0.205	1.83	0.809	0.489	0.395	2.43	7.583	0.34	0.5	0.205	1.83	0.809	0.489	0.395	2.61	8.255	0.36	0.56
0.205	1.83	0.809	0.489	0.395	2.74	7.982	0.34	0.54	0.205	1.83	0.809	0.489	0.395	2.86	7.79	0.35	0.54
0.205	1.83	0.809	0.489	0.395	2.99	7.596	0.32	0.52	0.205	1.83	0.809	0.489	0.395	3.12	8.067	0.38	0.55
0.205	1.83	0.809	0.489	0.395	3.25	7.788	0.33	0.55	0.205	1.83	0.809	0.489	0.395	3.39	8.1	0.35	0.59
0.205	1.83	0.809	0.489	0.395	3.52	7.88	0.36	0.57	0.205	1.83	0.809	0.489	0.395	3.72	7.382	0.3	0.52
0.223	1.97	0.799	0.496	0.385	2.38	6.513	0.28	0.43	0.223	1.97	0.799	0.496	0.385	2.55	6.614	0.28	0.43
0.223	1.97	0.799	0.496	0.385	2.68	6.038	0.27	0.4	0.223	1.97	0.799	0.496	0.385	2.81	6.66	0.3	0.45
0.223	1.97	0.799	0.496	0.385	2.96	6.588	0.3	0.44	0.223	1.97	0.799	0.496	0.385	3.12	6.341	0.27	0.39
0.223	1.97	0.799	0.496	0.385	3.27	6.855	0.31	0.47	0.223	1.97	0.799	0.496	0.385	3.41	6.75	0.31	0.47
0.223	1.97	0.799	0.496	0.385	3.55	6.31	0.29	0.45	0.223	1.97	0.799	0.496	0.385	3.75	6.956	0.3	0.48
0.256	2.21	0.782	0.507	0.37	2.17	4.856	0.14	0.34	0.256	2.21	0.782	0.507	0.37	2.35	4.648	0.13	0.31
0.256	2.21	0.782	0.507	0.37	2.48	5.105	0.16	0.34	0.256	2.21	0.782	0.507	0.37	2.6	5.215	0.17	0.35
0.256	2.21	0.782	0.507	0.37	2.74	5.025	0.16	0.34	0.256	2.21	0.782	0.507	0.37	2.93	4.618	0.15	0.32
0.256	2.21	0.782	0.507	0.37	3.16	5.046	0.16	0.3	0.256	2.21	0.782	0.507	0.37	3.38	5.051	0.17	0.36
0.256	2.21	0.782	0.507	0.37	3.57	4.536	0.14	0.33	0.256	2.21	0.782	0.507	0.37	3.83	4.27	0.091	0.31

TABLE VII. Unpolarized SIDIS cross sections in 2D bins for the π^+ channel. The data are presented in 10 groups, each of which has 10 bins of P_t, in one of the 10 ranges of x_{bj}. A group consists of five rows, and each row presents the information of two consecutive P_t bins. Nine columns are used to present the information of each bin: the central values of the kinematic variables, the differential cross section, and the uncertainties. A line is drawn in the middle of the table to separate the information of two bins in one row, for the convenience of reading.

x_{bj}	Q^2	y	z_h	P_t	ϕ_h	$d\sigma$	Stat.	Sys.	x_{bj}	Q^2	y	z_h	P_t	ϕ_h	$d\sigma$	Stat.	Sys.
0.164	1.5	0.825	0.48	0.36	3.11	26.34	1.5	1.6	0.164	1.5	0.825	0.48	0.378	3.11	24.07	1.3	1.6
0.164	1.5	0.825	0.48	0.391	3.11	20.47	1	1.4	0.164	1.5	0.825	0.48	0.404	3.11	19.32	0.98	1.4
0.164	1.5	0.825	0.48	0.416	3.11	18.93	0.96	1.3	0.164	1.5	0.825	0.48	0.428	3.11	16.92	0.86	1.2
0.164	1.5	0.825	0.48	0.44	3.11	15.54	0.79	1.1	0.164	1.5	0.825	0.48	0.453	3.11	17.26	0.81	1.2
0.164	1.5	0.825	0.48	0.467	3.11	14.33	0.73	1	0.164	1.5	0.825	0.48	0.49	3.11	12.23	0.52	1
0.19	1.71	0.814	0.487	0.335	3.08	18.79	1	1	0.19	1.71	0.814	0.487	0.357	3.08	19.6	1	1.2
0.19	1.71	0.814	0.487	0.371	3.08	15.51	0.75	0.91	0.19	1.71	0.814	0.487	0.385	3.08	14.88	0.71	0.89
0.19	1.71	0.814	0.487	0.398	3.08	15.38	0.76	0.92	0.19	1.71	0.814	0.487	0.41	3.08	16.47	0.79	1
0.19	1.71	0.814	0.487	0.423	3.08	13.37	0.63	0.81	0.19	1.71	0.814	0.487	0.436	3.08	14.11	0.69	0.85
0.19	1.71	0.814	0.487	0.449	3.08	14.14	0.68	0.87	0.19	1.71	0.814	0.487	0.472	3.08	11.2	0.49	0.79
0.209	1.86	0.804	0.492	0.314	3.08	17.83	0.93	1	0.209	1.86	0.804	0.492	0.338	3.08	16.07	0.77	0.92
0.209	1.86	0.804	0.492	0.353	3.08	13.83	0.68	0.8	0.209	1.86	0.804	0.492	0.366	3.08	13.82	0.68	0.8
0.209	1.86	0.804	0.492	0.378	3.08	13.33	0.65	0.77	0.209	1.86	0.804	0.492	0.39	3.08	13.82	0.65	0.79
0.209	1.86	0.804	0.492	0.403	3.08	11.41	0.53	0.66	0.209	1.86	0.804	0.492	0.417	3.08	11.28	0.52	0.64
0.209	1.86	0.804	0.492	0.432	3.08	11.48	0.53	0.67	0.209	1.86	0.804	0.492	0.458	3.08	10.01	0.42	0.65
0.227	1.99	0.794	0.499	0.291	3.08	14.96	0.79	0.91	0.227	1.99	0.794	0.499	0.316	3.08	13.16	0.69	0.74
0.227	1.99	0.794	0.499	0.332	3.08	11.94	0.58	0.67	0.227	1.99	0.794	0.499	0.347	3.08	10.47	0.51	0.57
0.227	1.99	0.794	0.499	0.36	3.08	11.48	0.56	0.68	0.227	1.99	0.794	0.499	0.372	3.08	11.85	0.56	0.65
0.227	1.99	0.794	0.499	0.384	3.08	10.77	0.52	0.6	0.227	1.99	0.794	0.499	0.397	3.08	10.79	0.49	0.61
0.227	1.99	0.794	0.499	0.412	3.08	9.563	0.46	0.54	0.227	1.99	0.794	0.499	0.44	3.08	8.39	0.34	0.5
0.245	2.11	0.781	0.507	0.271	3.06	13.5	0.73	0.78	0.245	2.11	0.781	0.507	0.297	3.06	10.26	0.53	0.6
0.245	2.11	0.781	0.507	0.314	3.06	10.58	0.51	0.6	0.245	2.11	0.781	0.507	0.328	3.06	11.52	0.58	0.68
0.245	2.11	0.781	0.507	0.34	3.06	10.2	0.52	0.53	0.245	2.11	0.781	0.507	0.352	3.06	10.48	0.52	0.57
0.245	2.11	0.781	0.507	0.365	3.06	8.899	0.42	0.5	0.245	2.11	0.781	0.507	0.379	3.06	10.52	0.49	0.58
0.245	2.11	0.781	0.507	0.394	3.06	8.806	0.42	0.49	0.245	2.11	0.781	0.507	0.425	3.06	8.986	0.37	0.52
0.264	2.24	0.769	0.515	0.247	3.09	10.62	0.57	0.66	0.264	2.24	0.769	0.515	0.274	3.09	9.329	0.46	0.58
0.264	2.24	0.769	0.515	0.292	3.09	8.852	0.43	0.53	0.264	2.24	0.769	0.515	0.307	3.09	8.249	0.4	0.48
0.264	2.24	0.769	0.515	0.321	3.09	8.493	0.39	0.49	0.264	2.24	0.769	0.515	0.334	3.09	8.379	0.41	0.51
0.264	2.24	0.769	0.515	0.346	3.09	8.113	0.4	0.48	0.264	2.24	0.769	0.515	0.359	3.09	7.779	0.37	0.45
0.264	2.24	0.769	0.515	0.375	3.09	8.01	0.37	0.47	0.264	2.24	0.769	0.515	0.407	3.09	6.983	0.28	0.4
0.285	2.37	0.755	0.524	0.221	3.07	9.644	0.5	0.61	0.285	2.37	0.755	0.524	0.25	3.07	8.818	0.42	0.6
0.285	2.37	0.755	0.524	0.268	3.07	7.823	0.38	0.48	0.285	2.37	0.755	0.524	0.283	3.07	7.046	0.36	0.43
0.285	2.37	0.755	0.524	0.297	3.07	7.482	0.34	0.47	0.285	2.37	0.755	0.524	0.31	3.07	7.382	0.36	0.43
0.285	2.37	0.755	0.524	0.323	3.07	6.446	0.3	0.38	0.285	2.37	0.755	0.524	0.337	3.07	7.356	0.35	0.46
0.285	2.37	0.755	0.524	0.352	3.07	6.807	0.34	0.42	0.285	2.37	0.755	0.524	0.385	3.07	6.245	0.24	0.38
0.308	2.52	0.739	0.536	0.193	3.07	8.177	0.39	0.5	0.308	2.52	0.739	0.536	0.223	3.07	7.161	0.34	0.46
0.308	2.52	0.739	0.536	0.242	3.07	7.528	0.34	0.46	0.308	2.52	0.739	0.536	0.257	3.07	6.659	0.31	0.42
0.308	2.52	0.739	0.536	0.271	3.07	6.947	0.31	0.46	0.308	2.52	0.739	0.536	0.285	3.07	6.056	0.27	0.38
0.308	2.52	0.739	0.536	0.299	3.07	5.84	0.27	0.37	0.308	2.52	0.739	0.536	0.314	3.07	5.786	0.26	0.38
0.308	2.52	0.739	0.536	0.331	3.07	5.641	0.25	0.34	0.308	2.52	0.739	0.536	0.368	3.07	5.696	0.22	0.35
0.336	2.68	0.722	0.549	0.161	3.1	5.965	0.29	0.38	0.336	2.68	0.722	0.549	0.195	3.1	5.128	0.23	0.34
0.336	2.68	0.722	0.549	0.214	3.1	5.22	0.25	0.33	0.336	2.68	0.722	0.549	0.229	3.1	5.272	0.25	0.33
0.336	2.68	0.722	0.549	0.243	3.1	5.021	0.23	0.32	0.336	2.68	0.722	0.549	0.257	3.1	5.141	0.24	0.33
0.336	2.68	0.722	0.549	0.271	3.1	5.085	0.23	0.35	0.336	2.68	0.722	0.549	0.286	3.1	5.428	0.24	0.36
0.336	2.68	0.722	0.549	0.304	3.1	5.161	0.23	0.33	0.336	2.68	0.722	0.549	0.343	3.1	4.42	0.16	0.28
0.381	2.96	0.704	0.562	0.122	3.05	4.665	0.19	0.35	0.381	2.96	0.704	0.562	0.155	3.05	4.346	0.17	0.36
0.381	2.96	0.704	0.562	0.175	3.05	4.128	0.16	0.33	0.381	2.96	0.704	0.562	0.192	3.05	4.356	0.16	0.37
0.381	2.96	0.704	0.562	0.207	3.05	4.13	0.16	0.34	0.381	2.96	0.704	0.562	0.221	3.05	4.455	0.16	0.37
0.381	2.96	0.704	0.562	0.236	3.05	3.989	0.15	0.35	0.381	2.96	0.704	0.562	0.253	3.05	3.558	0.13	0.31
0.381	2.96	0.704	0.562	0.272	3.05	3.516	0.13	0.31	0.381	2.96	0.704	0.562	0.316	3.05	3.496	0.11	0.33

TABLE VIII. Unpolarized SIDIS cross sections in 2D bins for the π^- channel. The format is the same as the previous table for the π^+ channel.

x_{bj}	Q^2	y	z_h	P_t	ϕ_h	$d\sigma$	Stat.	Sys.	x_{bj}	Q^2	y	z_h	P_t	ϕ_h	$d\sigma$	Stat.	Sys.
0.164	1.5	0.825	0.48	0.36	3.11	18.42	0.99	1.2	0.164	1.5	0.825	0.48	0.378	3.11	16.67	0.86	1.2
0.164	1.5	0.825	0.48	0.391	3.11	13.39	0.59	1	0.164	1.5	0.825	0.48	0.404	3.11	11.7	0.51	0.89
0.164	1.5	0.825	0.48	0.416	3.11	10.98	0.46	0.83	0.164	1.5	0.825	0.48	0.428	3.11	10.04	0.43	0.75
0.164	1.5	0.825	0.48	0.44	3.11	9.779	0.42	0.73	0.164	1.5	0.825	0.48	0.453	3.11	9.9	0.38	0.72
0.164	1.5	0.825	0.48	0.467	3.11	9.662	0.44	0.74	0.164	1.5	0.825	0.48	0.49	3.11	8.378	0.31	0.7
0.19	1.71	0.814	0.487	0.335	3.08	13.14	0.65	0.82	0.19	1.71	0.814	0.487	0.357	3.08	12.05	0.54	0.8
0.19	1.71	0.814	0.487	0.371	3.08	10.79	0.48	0.71	0.19	1.71	0.814	0.487	0.385	3.08	9.442	0.39	0.64
0.19	1.71	0.814	0.487	0.398	3.08	10.11	0.45	0.68	0.19	1.71	0.814	0.487	0.41	3.08	8.966	0.35	0.6
0.19	1.71	0.814	0.487	0.423	3.08	8.546	0.35	0.57	0.19	1.71	0.814	0.487	0.436	3.08	8.429	0.35	0.56
0.19	1.71	0.814	0.487	0.449	3.08	7.746	0.3	0.53	0.19	1.71	0.814	0.487	0.472	3.08	7.314	0.28	0.54
0.209	1.86	0.804	0.491	0.314	3.08	10.65	0.49	0.67	0.209	1.86	0.804	0.491	0.338	3.08	8.655	0.35	0.56
0.209	1.86	0.804	0.491	0.353	3.08	8.671	0.38	0.57	0.209	1.86	0.804	0.491	0.366	3.08	7.718	0.32	0.51
0.209	1.86	0.804	0.491	0.378	3.08	8.551	0.37	0.57	0.209	1.86	0.804	0.491	0.39	3.08	8.066	0.32	0.52
0.209	1.86	0.804	0.491	0.403	3.08	7.268	0.29	0.48	0.209	1.86	0.804	0.491	0.417	3.08	6.871	0.27	0.45
0.209	1.86	0.804	0.491	0.432	3.08	6.267	0.23	0.42	0.209	1.86	0.804	0.491	0.458	3.08	5.94	0.2	0.42
0.227	1.99	0.794	0.498	0.291	3.08	8.909	0.41	0.56	0.227	1.99	0.794	0.498	0.316	3.08	9.172	0.45	0.59
0.227	1.99	0.794	0.498	0.332	3.08	7.514	0.32	0.49	0.227	1.99	0.794	0.498	0.347	3.08	7.359	0.33	0.48
0.227	1.99	0.794	0.498	0.36	3.08	6.392	0.26	0.41	0.227	1.99	0.794	0.498	0.372	3.08	6.896	0.28	0.44
0.227	1.99	0.794	0.498	0.384	3.08	7.082	0.31	0.46	0.227	1.99	0.794	0.498	0.397	3.08	5.912	0.22	0.39
0.227	1.99	0.794	0.498	0.412	3.08	6.607	0.29	0.42	0.227	1.99	0.794	0.498	0.44	3.08	4.884	0.16	0.32
0.245	2.11	0.781	0.507	0.271	3.06	8.322	0.4	0.53	0.245	2.11	0.781	0.507	0.297	3.06	6.505	0.3	0.44
0.245	2.11	0.781	0.507	0.314	3.06	6.682	0.29	0.44	0.245	2.11	0.781	0.507	0.328	3.06	6.776	0.3	0.45
0.245	2.11	0.781	0.507	0.34	3.06	6.682	0.31	0.43	0.245	2.11	0.781	0.507	0.352	3.06	6.197	0.26	0.41
0.245	2.11	0.781	0.507	0.365	3.06	5.828	0.25	0.38	0.245	2.11	0.781	0.507	0.379	3.06	5.559	0.21	0.36
0.245	2.11	0.781	0.507	0.394	3.06	5.139	0.2	0.33	0.245	2.11	0.781	0.507	0.425	3.06	4.673	0.15	0.3
0.264	2.24	0.769	0.515	0.247	3.09	7.03	0.34	0.47	0.264	2.24	0.769	0.515	0.274	3.09	5.788	0.25	0.39
0.264	2.24	0.769	0.515	0.292	3.09	5.678	0.25	0.38	0.264	2.24	0.769	0.515	0.307	3.09	5.4	0.23	0.37
0.264	2.24	0.769	0.515	0.321	3.09	5.122	0.2	0.34	0.264	2.24	0.769	0.515	0.334	3.09	4.738	0.2	0.32
0.264	2.24	0.769	0.515	0.346	3.09	5.25	0.23	0.36	0.264	2.24	0.769	0.515	0.359	3.09	4.581	0.19	0.3
0.264	2.24	0.769	0.515	0.375	3.09	4.161	0.15	0.28	0.264	2.24	0.769	0.515	0.407	3.09	3.952	0.13	0.26
0.284	2.37	0.755	0.524	0.221	3.07	5.468	0.25	0.36	0.284	2.37	0.755	0.524	0.25	3.07	4.766	0.19	0.33
0.284	2.37	0.755	0.524	0.268	3.07	4.425	0.18	0.31	0.284	2.37	0.755	0.524	0.283	3.07	4.722	0.21	0.33
0.284	2.37	0.755	0.524	0.297	3.07	3.927	0.15	0.27	0.284	2.37	0.755	0.524	0.31	3.07	4.239	0.17	0.29
0.284	2.37	0.755	0.524	0.323	3.07	4.3	0.18	0.3	0.284	2.37	0.755	0.524	0.337	3.07	3.641	0.14	0.25
0.284	2.37	0.755	0.524	0.352	3.07	4.377	0.19	0.3	0.284	2.37	0.755	0.524	0.385	3.07	3.491	0.11	0.24
0.308	2.52	0.74	0.536	0.193	3.07	4.535	0.18	0.31	0.308	2.52	0.74	0.536	0.223	3.07	4.266	0.18	0.3
0.308	2.52	0.74	0.536	0.242	3.07	4.076	0.16	0.29	0.308	2.52	0.74	0.536	0.257	3.07	3.858	0.15	0.28
0.308	2.52	0.74	0.536	0.271	3.07	3.519	0.13	0.25	0.308	2.52	0.74	0.536	0.285	3.07	3.58	0.14	0.26
0.308	2.52	0.74	0.536	0.299	3.07	3.271	0.12	0.23	0.308	2.52	0.74	0.536	0.314	3.07	3.046	0.11	0.22
0.308	2.52	0.74	0.536	0.331	3.07	2.705	0.094	0.19	0.308	2.52	0.74	0.536	0.368	3.07	2.972	0.091	0.21
0.336	2.68	0.722	0.548	0.161	3.1	3.508	0.14	0.24	0.336	2.68	0.722	0.548	0.195	3.1	2.964	0.11	0.21
0.336	2.68	0.722	0.548	0.214	3.1	3.319	0.14	0.24	0.336	2.68	0.722	0.548	0.229	3.1	3.235	0.14	0.23
0.336	2.68	0.722	0.548	0.243	3.1	2.994	0.12	0.22	0.336	2.68	0.722	0.548	0.257	3.1	2.565	0.094	0.19
0.336	2.68	0.722	0.548	0.271	3.1	2.585	0.096	0.19	0.336	2.68	0.722	0.548	0.286	3.1	2.293	0.074	0.17
0.336	2.68	0.722	0.548	0.304	3.1	2.579	0.09	0.19	0.336	2.68	0.722	0.548	0.343	3.1	2.416	0.072	0.17
0.38	2.96	0.705	0.561	0.122	3.05	3.01	0.11	0.27	0.38	2.96	0.705	0.561	0.155	3.05	2.238	0.068	0.21
0.38	2.96	0.705	0.561	0.175	3.05	2.398	0.077	0.24	0.38	2.96	0.705	0.561	0.192	3.05	2.295	0.068	0.23
0.38	2.96	0.705	0.561	0.207	3.05	2.321	0.074	0.23	0.38	2.96	0.705	0.561	0.221	3.05	2.332	0.069	0.24
0.38	2.96	0.705	0.561	0.236	3.05	1.915	0.053	0.2	0.38	2.96	0.705	0.561	0.253	3.05	2.003	0.061	0.21
0.38	2.96	0.705	0.561	0.272	3.05	1.889	0.058	0.2	0.38	2.96	0.705	0.561	0.316	3.05	1.713	0.039	0.2

Azimuthal modulations in unpolarized SIDIS are observed to be consistent with zero within the experimental uncertainties in this study. Using the specific functional form as in the global analysis [15], the fitting results show that the width of quark intrinsic transverse momentum $\langle k_\perp^2 \rangle$ is much smaller than the results from the global analyses of other types of data [5,15–17]. With relaxed model formulation, $\langle k_\perp^2 \rangle$ and $\langle p_\perp^2 \rangle$ are under looser constraint individually, while the combined quantity $\langle P_t^2 \rangle$ is constrained by the P_t behavior of the data. The widths $\langle k_\perp^2 \rangle$ and $\langle p_\perp^2 \rangle$ in the structure functions, related to the azimuthal modulations are determined consistently by using the extracted cross sections with and without the information of ϕ_h.

Apparently, a simple model at the lowest twist was able to describe the main features of the data. The applicability of the simple model to semi-inclusive experiments on the proton and deuteron targets in modest Q^2 ranges was also observed by other JLab experiments [22,23]. While one might naively expect large contributions from the higher-twist terms in the modest Q^2 range, they have not been found to be significant experimentally. It is possible that the contributions of the higher-twist terms in the SIDIS process are not as large as expected. It is also possible that the higher-twist contributions have been absorbed into the lowest-twist model by changing the parameters ($\langle k_\perp^2 \rangle$ and $\langle p_\perp^2 \rangle$). On the other hand, besides the general agreement between the simple model and the data in this study, sizable differences exist in some of the kinematic ranges. These differences might be related to the higher-twist terms.

Clearly, high-precision data in the modest Q^2 range with a full azimuthal angular coverage will, in addition to study the leading-twist TMDs, provide opportunities to study the details of the higher-twist terms and their effects on the azimuthal angular modulations. The future 12 GeV SIDIS programs at JLab with SoLID combining high luminosities and a large acceptance including a full azimuthal angular coverage [61,62] will provide high-precision data of the SIDIS differential cross sections as well as the azimuthal modulations in multidimensional bins covering a broad kinematic range. These data will significantly advance the development of the TMD phenomenology and our understanding of the TMD physics.

ACKNOWLEDGMENTS

We acknowledge the outstanding support of the JLab Hall A staff and the Accelerator Division in accomplishing this experiment. This work was supported in part by the US National Science Foundation, and by Department of Energy (DOE) contract number DE-AC05-06OR23177, under which the Jefferson Science Associates operates the Thomas Jefferson National Accelerator Facility. This work was also supported in part by the US Department of Energy under Contract DE-FG02-03ER41231 and the National Natural Science Foundation of China No. 11120101004.

APPENDIX: SEMI-INCLUSIVE DEEP-INELASTIC SCATTERING CROSS-SECTION DATA TABLE

The SIDIS differential cross sections in pseudo-1D, 2D, and 3D bins and the corresponding kinematic variables are presented in the tables below.

The units of quantities are as the following: Q^2 is in unit of GeV^2, P_t in unit of GeV, ϕ_h in unit of rad. Symbol $d\sigma$ stands for $d\sigma/(dx_{bj}dydz_hd\phi_S dP_t^2 d\phi_h)$ in unit of nb GeV^{-2} rad^{-2}. Abbreviations Stat. and Sys. stand for statistical and systematic uncertainties, respectively, in unit of nb GeV^{-2} rad^{-2}.

---

[1] M. Arneodo *et al.* (European Muon Collaboration), Z. Phys. C: Part. Fields **34**, 277 (1987).

[2] A. Airapetian *et al.* (HERMES Collaboration), Phys. Rev. Lett. **94**, 012002 (2005).

[3] V. Yu. Alexakhin *et al.* (COMPASS Collaboration), Phys. Rev. Lett. **94**, 202002 (2005).

[4] H. Avakian *et al.* (CLAS Collaboration), Phys. Rev. D **69**, 112004 (2004).

[5] M. Anselmino, M. Boglione, U. D'Alesio, A. Kotzinian, F. Murgia, and A. Prokudin, Phys. Rev. D **71**, 074006 (2005).

[6] M. Anselmino, A. Efremov, A. Kotzinian, and B. Parsamyan, Phys. Rev. D **74**, 074015 (2006).

[7] P. J. Mulders and R. D. Tangerman, Nucl. Phys. B **461**, 197 (1996); **484**, 538 (1997).

[8] D. Boer and P. J. Mulders, Phys. Rev. D **57**, 5780 (1998).

[9] J. C. Collins, D. E. Soper, and G. F. Sterman, Nucl. Phys. B **250**, 199 (1985).

[10] S. J. Brodsky, D. S. Hwang, and I. Schmidt, Phys. Lett. B **530**, 99 (2002).

[11] X.-d. Ji, J.-P. Ma, and F. Yuan, Phys. Lett. B **597**, 299 (2004).

[12] S. M. Aybat and T. C. Rogers, Phys. Rev. D **83**, 114042 (2011).

[13] A. Bacchetta, M. Diehl, K. Goeke, A. Metz, P. J. Mulders, and M. Schlegel, J. High Energy Phys. 02 (2007) 093.

[14] V. Barone, F. Bradamante, and A. Martin, Prog. Part. Nucl. Phys. **65**, 267 (2010).

[15] V. Barone, M. Boglione, J.O. Gonzalez Hernandez, and S. Melis, Phys. Rev. D **91**, 074019 (2015).

[16] M. Anselmino, M. Boglione, J. O. Gonzalez Hernandez, S. Melis, and A. Prokudin, J. High Energy Phys. 04 (2014) 005.

[17] A. Bacchetta and M. Radici, Phys. Rev. Lett. **107**, 212001 (2011).

[18] R. N. Cahn, Phys. Lett. B **78**, 269 (1978).

[19] J. Collins, *Foundations of Perturbative QCD* (Cambridge University Press, New York, 2013).

[20] K. A. Olive *et al.* (Particle Data Group), Chin. Phys. C **38**, 090001 (2014).

[21] S. Kuhn, J.-P. Chen, and E. Leader, Prog. Part. Nucl. Phys. **63**, 1 (2009).

[22] R. Asaturyan *et al.*, Phys. Rev. C **85**, 015202 (2012).

[23] M. Osipenko *et al.* (CLAS Collaboration), Phys. Rev. D **80**, 032004 (2009).

[24] A. Airapetian *et al.* (HERMES Collaboration), Phys. Rev. D **87**, 074029 (2013).

[25] C. Adolph *et al.* (COMPASS Collaboration), Eur. Phys. J. C **73**, 2531 (2013).

[26] A. Airapetian *et al.* (HERMES Collaboration), Phys. Rev. D **87**, 012010 (2013).
[27] C. Adolph *et al.* (COMPASS Collaboration), Nucl. Phys. B **886**, 1046 (2014).
[28] J. L. Friar, B. F. Gibson, G. L. Payne, A. M. Bernstein, and T. E. Chupp, Phys. Rev. C **42**, 2310 (1990).
[29] X. Qian *et al.*, Phys. Rev. Lett. **107**, 072003 (2011).
[30] J. Huang *et al.*, Phys. Rev. Lett. **108**, 052001 (2012).
[31] Y. Zhang *et al.*, Phys. Rev. C **90**, 055209 (2014).
[32] Y. X. Zhao *et al.*, Phys. Rev. C **90**, 055201 (2014).
[33] M. Anselmino, Few-Body Syst. **57**, 373 (2016).
[34] A. Martin, Int. J. Mod. Phys.: Conf. Ser. **40**, 1660028 (2016).
[35] A. Bacchetta, U. D'Alesio, M. Diehl, and C. A. Miller, Phys. Rev. D **70**, 117504 (2004).
[36] A. Signori, A. Bacchetta, M. Radici, and G. Schnell, J. High Energy Phys. 11 (2013) 194.
[37] D. J. J. de Lange *et al.*, Nucl. Instrum. Methods Phys. Res., Sect. A **406**, 182 (1998).
[38] D. J. J. de Lange *et al.*, Nucl. Instrum. Methods Phys. Res., Sect. A **412**, 254 (1998).
[39] M. Mihovilovic *et al.*, Nucl. Instrum. Methods Phys. Res., Sect. A **686**, 20 (2012).
[40] J. Alcorn *et al.*, Nucl. Instrum. Methods Phys. Res., Sect. A **522**, 294 (2004).
[41] W. Happer, Rev. Mod. Phys. **44**, 169 (1972).
[42] X. Qian, Ph.D. thesis, Duke University, 2011 (unpublished).
[43] K. Allada *et al.*, Phys. Rev. C **89**, 042201 (2014).
[44] J. Huang, Ph.D. thesis, Massachusetts Institute of Technology, 2012 (unpublished).
[45] Hall C Monte Carlo Package for SIDIS, https://hallcweb.jlab.org/wiki/index.php/Monte_Carlo
[46] SIMC for E06-010, https://userweb.jlab.org/puckett/e06010/simc_transversity_documentation.pdf
[47] R. Bradford, A. Bodek, H. S. Budd, and J. Arrington, Nucl. Phys. B, Proc. Suppl. **159**, 127 (2006).
[48] I. Akushevich, H. Gao, A. Ilyichev, and M. Meziane, Eur. Phys. J. A **51**, 1 (2015).
[49] P. E. Bosted and V. Mamyan, arXiv:1203.2262.
[50] D. Flay *et al.* (Jefferson Lab Hall A Collaboration), Phys. Rev. D **94**, 052003 (2016).
[51] D. Flay, Ph.D. thesis, Temple University, 2014 (unpublished).
[52] L. W. Mo and Y.-S. Tsai, Rev. Mod. Phys. **41**, 205 (1969).
[53] I. Akushevich, A. Ilyichev, N. Shumeiko, A. Soroko, and A. Tolkachev, Comput. Phys. Commun. **104**, 201 (1997).
[54] J. W. Lightbody and J. S. O'Connel, Comput. Phys. **2**, 57 (1988).
[55] I. Akushevich, A. Ilyichev, and M. Osipenko, Phys. Lett. B **672**, 35 (2009).
[56] T. Sjostrand, S. Mrenna, and P. Z. Skands, J. High Energy Phys. 05 (2006) 026.
[57] H. Avakian *et al.* (CLAS Collaboration), Phys. Rev. Lett. **105**, 262002 (2010).
[58] H.-L. Lai, M. Guzzi, J. Huston, Z. Li, P. M. Nadolsky, J. Pumplin, and C. P. Yuan, Phys. Rev. D **82**, 074024 (2010).
[59] D. de Florian, R. Sassot, and M. Stratmann, Phys. Rev. D **75**, 114010 (2007).
[60] L. L. Pappalardo, Ph.D. thesis, Univsity of Ferrara, 2008 (unpublished).
[61] H. Gao *et al.*, Eur. Phys. J. Plus **126**, 2 (2011).
[62] J.-P. Chen *et al.*, arXiv:1409.7741.